https://doi.org/10.5194/egusphere-2025-3788
Preprint. Discussion started: 15 August 2025

Accelerated lowland thermokarst development revealed by UAS photogrammetric surveys in the Stordalen mire, Abisko, Sweden

Maxime Thomas[1], Thomas Moenaert[1], Julien Radoux[1], Baptiste Delhez[1], Eléonore du Bois d'Aische[1], Maëlle Villani[1], Catherine Hirst[1,2], Erik Lundin[3], François Jonard[4], Sébastien Lambot[1], Kristof Van Oost[1], Veerle Vanacker[1], Matthias B. Siewert[5], Carl-Magnus Mörth[6], Michael W. Palace[7], Ruth K. Varner[6,7], Franklin B. Sullivan[8], Christina Herrick[8], Sophie Opfergelt[1]

[1]Earth and Life Institute, Université catholique de Louvain, Louvain-la-Neuve, Belgium
[2]Department of Earth Sciences, Durham University, Durham, United Kingdom
[3]Abisko Scientific Research Station, Swedish Polar Research Secretariat, Abisko, Sweden
[4]Earth Observation and Ecosystem Modelling Laboratory, Université de Liège, Liège, Belgium
[5]Department of Ecology and Environmental Science, Umeå University, Umeå, Sweden
[6]Department of Geological Sciences, Stockholm University, Stockholm, Sweden
[7]Department of Earth Sciences and Institute for the Study of Earth, Oceans and Space, University of New Hampshire, Durham, NH USA
[8]Earth Systems Research Center, Institute for the Study of Earth, Oceans and Space, University of New Hampshire, Durham, NH USA

Correspondence to: Maxime Thomas (maxime.thomas@uclouvain.be)

Abstract. The estimation of greenhouse gas (GHG) emissions from permafrost soils is challenging, as organic matter propensity to decompose depends on factors such as soil pH, temperature, and redox conditions. Over lowland permafrost soils, these conditions are directly related to the microtopography and evolve with physical degradation, i.e., lowland thermokarst development (i.e., a local collapse of the land surface due to ice-rich permafrost thaw). A dynamic quantification of thermokarst development – still poorly constrained – is therefore a critical prerequisite for predictive models of permafrost carbon balance in these areas. This requires high-resolution mapping, as lowland thermokarst development induces fine-scale spatial variability (~50 – 100 cm). Here we provide such a quantification, updated for the Stordalen mire in Abisko, Sweden for the Stordalen mire, Abisko, Sweden (68°21'20"N 19°02'38"E), which displays a gradient from well-drained stable palsas to inundated fens, which have undergone ground subsidence. We produced RGB orthomosaics and digital elevation models from very high resolution (10 cm) unoccupied aircraft system (UAS) photogrammetry as well as a spatially continuous map of soil electrical conductivity (EC) based on electromagnetic induction (EMI) measurements. We classified the land cover following the degradation gradient and derived palsa loss rates. Our findings confirm that topography is an essential parameter for determining the evolution of palsa degradation, enhancing the overall accuracy of the classification from 41% to 77%, with the addition of slope allowing the detection of the early stages of degradation. We show a clear acceleration of degradation for the period 2019 – 2021, with a decrease in palsa area of 0.9 – 1.1%·a^{-1} (% reduction per year relative to the entire mire) compared to previous estimates of ~0.2%·a^{-1} (1970 – 2000) and ~0.04%·a^{-1} (2000 – 2014). EMI data show that this degradation leads to an increase in soil moisture, which in turn likely decreases organic carbon geochemical stability and

https://doi.org/10.5194/egusphere-2025-3788
Preprint. Discussion started: 15 August 2025

potentially increases methane emissions. With a palsa loss of 0.9 – 1.1%·a^{-1}, we estimate accordingly that surface degradation at Stordalen might lead to a pool of 12 metric tons of organic carbon exposed annually for the topsoil (23 cm depth), of which ~25% is mineral-interacting organic carbon. Likewise, average annual emissions would increase from ~ 7.1 g-C·m^{-2}·a^{-1} in 2019 to ~ 7.3 g-C·m^{-2}·a^{-1} in 2021 for the entire mire, i.e., an increase of ~1.3%·a^{-1}. As topography changes due to lowland thermokarst are fine-scaled and thus not possible to detect from satellite images, circumpolar up-scaling assessments are challenging. By extending the monitoring we have conducted as part of this study to other lowland areas, it would be possible to assess the spatial variability of palsa degradation/thermokarst formation rates and thus improve estimates of net ecosystem carbon dynamics.

1 Introduction

Arctic air temperature is increasing three to four times faster than the global average increase (AMAP, 2021; Rantanen et al., 2022) and we are consequently anticipating the near-surface permafrost area to decrease by 2 – 66% for Intergovernmental Panel on Climate Change (IPCC) scenario RCP2.6 and 30 – 99% for RCP8.5, by 2100 (Fox-Kemper et al., 2021; Meredith et al., 2019). Arctic and boreal permafrost region soils and sediments store 1460 – 1600 Gt of organic carbon (OC; Hugelius et al., 2014; Strauss et al., 2021), which could release 3 – 41 petagram of carbon as CO_2 per 1ºC of global warming by 2100, with high confidence to produce a positive feedback and accelerate climate change (Canadell et al., 2021). In particular, northern peatlands, which have historically acted as carbon sinks, are expected to turn into carbon sources, with a projected thaw leading to greenhouse gas (GHG) emissions equivalent to ~1% of anthropogenic radiative forcing in this century (Hugelius et al., 2020).

As the permafrost thaws, excess ground ice melts, along with its associated cementing properties, resulting in surface subsidence. This phenomenon is widespread across the arctic permafrost region, with thaw subsidence rates of up to 2 cm·a^{-1} in the areas with low ice content and more than 3 cm·a^{-1} in regions with ice-rich permafrost (Streletskiy et al., 2025). In the particular areas with large amounts of excess ground ice, we often refer to the development of thermokarst landforms (e.g., Heginbottom et al., 2012; Kokelj and Jorgenson, 2013), or abrupt thaw (Turetsky et al., 2020) which are physical degradations of the landscape that occur when the ground subsides or collapses with significant consequences for hydrologic and biogeochemical cycles. The development of thermokarst landforms is not included in the IPCC models of permafrost GHG emissions, yet they constitute nonlinear processes which are expected to intensify and compromise the feasibility of remaining below 1.5°C or 2°C targeted by the Paris Agreement (Natali et al., 2021). The estimation of GHG emissions from such landscapes is challenging, as organic matter propensity to decompose depends on factors such as the soil pH, temperature and redox conditions (e.g., Arndt et al., 2013; Canfield, 1994; Hemingway et al., 2019; Keil and Mayer, 2014; Lehmann and Kleber, 2015; von Lützow et al., 2008; Li et al., 2023), the latter of which may change drastically following certain thermokarst developments. Under the SSP58.5 scenario (the Shared Socio-economic Pathway (SSP) corresponding to very high greenhouse gas emissions scenario; Fox-Kemper et al., 2021), GHG emissions across 2.5 million km^2 of thermokarst landforms could

https://doi.org/10.5194/egusphere-2025-3788
Preprint. Discussion started: 15 August 2025

provide an additional and comparable feedback as gradual thaw emissions (Turetsky et al., 2020). These assessments are calculated via cumulative net ecosystem carbon balance (NECB) estimates – calculated for different models of abrupt thaw succession – which become increasingly negative and directly influenced by the rate of permafrost degradation (transition rate; Bosiö et al., 2012; Turetsky et al., 2020).

The approach used to estimate the rate of development of a thermokarst landscape depends on the type of degradation. Although dozens of thermokarst types have been described in the literature (e.g., Barry and Hall-McKim, 2018; Burn and Lewkowicz, 1990; Farquharson et al., 2019; Godin and Fortier, 2012; Heginbottom et al., 2012; Kokelj et al., 2021; Kokelj and Jorgenson, 2013; Lamoureux and Lafrenière, 2009; Lewkowicz, 2007; Lewkowicz and Way, 2019; Olefeldt et al., 2016; Patzner et al., 2020; Vonk et al., 2015), we generally consider three main models: (i) hillslope/upland landscapes where physical degradation leads to slumps, active layer detachments and gullies; (ii) lowland mineral landscapes characterized by the formation of thaw lakes, and (iii) lowland organic-rich landscapes with the formation of thaw lakes or wetlands (Turetsky et al., 2020).

Nitze et al. (2018) recently quantified the abundance of different types of disturbances at the Arctic scale, namely (i) lake area loss, (ii) fires and (iii) thaw slumps. Still, the reported study techniques only allow mapping of relatively large features (i.e. several tens of meters). The detection of hillslope thermokarst landscapes is possible using satellite remote sensing (e.g., Kokelj et al., 2017; Lantz and Kokelj, 2008; Yang et al., 2023 for monitoring thaw slumps) but remains challenging due to the highly dynamic nature and sometimes fine scale[1] of those disturbances. Unoccupied aircraft system (UAS) technology makes it easier to detect such changes (e.g., de la Barreda-Bautista et al., 2022; Palace et al., 2018; van der Sluijs et al., 2023, 2018), as it allows for the collection of imagery with both high temporal and spatial resolutions.

For lowland organic landscapes where thermokarst development leads to the formation of thaw lakes or wetlands, the temporal evolution of degradation is even more complicated to study, since landscape deformations occur on very subtle spatial scales, i.e. only a few tens of centimeters per year, both horizontally and vertically or several meters lateral erosion per decade (de la Barreda-Bautista et al., 2022). Therefore, few studies have been devoted to quantifying this type of physical degradation by using remotely sensed image data. Reported rates of degradation are extremely variable, i.e., range from $0.04\%\cdot a^{-1}$ to $0.7\%\cdot a^{-1}$ (% reduction per year) of total land cover area (Chasmer and Hopkinson, 2017; Christensen et al., 2004; Rodenhizer et al., 2022; Turetsky et al., 2020; Varner et al., 2022). This degradation and associated subsidence are most pronounced in the lateral zones of stable permafrost patches (Borge et al., 2017; Mamet et al., 2017; Martin et al., 2021; Olvmo et al., 2020; Renette et al., 2024). Studies further showed that degradation is observed over larger regions, with 55% of Sweden's largest palsa peatlands currently subsiding (Valman et al., 2024). A few studies suggest an accelerated rate of degradation in more recent years (de la Barreda-Bautista et al., 2022; Borge et al., 2017; Olvmo et al., 2020), but still require at least ten years of survey data to enable palsa loss detection.

[1] Over the Peel Plateau, Canada, for instance, scar zones range in size from < 1 ha to ~ 33 ha (Brooker et al., 2014; Kokelj et al., 2021; Lacelle et al., 2015; Littlefair et al., 2017; Malone et al., 2013; Zolkos et al., 2018; Zolkos and Tank, 2019, 2020).

https://doi.org/10.5194/egusphere-2025-3788
Preprint. Discussion started: 15 August 2025

In this study, we revisit the quantification of the rate of palsa degradation between the summers of 2019 and 2021 in the Stordalen mire (Abisko, Sweden) using UAS-based photogrammetric surveys. We combine surface properties (obtained from color imagery/RGB orthomosaics) with information on micro-topography (relative elevation and slope obtained from digital surface models) to track the physical degradation of palsa over a two-year period. This enables a short-term quantification of palsa loss rates. We then widen our analysis to cover the years 2014 to 2022 by linking the physical degradation of the landscape with variation in open water areas. Additionally, we use electromagnetic induction (EMI) on a smaller extent to map soil electrical conductivity and infer contrasts in redox conditions, allowing for comparison with topography, orthophoto-derived vegetation patterns, and classification model results. Ultimately, we use the generated thematic maps to scale up organic carbon stocks, stability and release in the palsa mire. This multi-scale approach aims to improve our understanding of the dynamics of lowland thermokarst development and support future modeling of permafrost-related carbon feedbacks.

2 Methods

2.1 Study area and site description

The Stordalen Mire (68°21'20"N 19°02'38"E) is a peatland located approximately 10 km southeast of the town of Abisko in northern Sweden. Permafrost is sporadic in the region and confined to peatlands in valley bottoms and to mountain tops. The mean annual air temperature measured at the Abisko Scientific Research Station (~10 km from Stordalen) has risen by 2.5 °C from 1913 to 2006 and reached the value of 0.6°C in 2006 (Callaghan et al., 2010). The Stordalen mire consists of three distinct sub-habitats which represent a gradient of permafrost degradation (**Fig. 1a-b**; **Fig. A. 1a**). Those three sub-habitats are common to northern wetlands: (i) a well-drained raised palsa with a permafrost core (active layer depth of ~ 50 cm in 2021), dominated by ericaceous and woody plants, which is referred to as stable palsa, (ii) palsa undergoing active degradation with fluctuating water table depth and some active thawing, dominated by *Eriphorum spp.* and *Sphagnum spp.*, which is referred to as a palsa undergoing degradation and (iii) a fully thawed and inundated fen which has undergone full ground subsidence, indicated by the presence of sedges such as *Eriophorum Spp.* and which is referred to as highly degraded (de la Barreda-Bautista et al., 2022; Siewert, 2018; Sjögersten et al., 2023). The area also includes open water ponds formed during permafrost thaw (Burke et al., 2019; Chang et al., 2019b, a; Hodgkins et al., 2014; Johansson et al., 2006; Mondav et al., 2014; Patzner et al., 2020). As an illustration, measurements within an extent of less than 10 m² (**Fig. A. 1a**) reveal that the active layer depth varies from 50 cm to more than 200 cm from stable palsa to degraded areas (likely reflecting a complete thaw of permafrost at depth; **Fig. A. 1b**) and soil volumetric water content varies accordingly from 20% to 60% (**Fig. A. 1c**, based on METER TEROS 12 probes measurements).

https://doi.org/10.5194/egusphere-2025-3788
Preprint. Discussion started: 15 August 2025

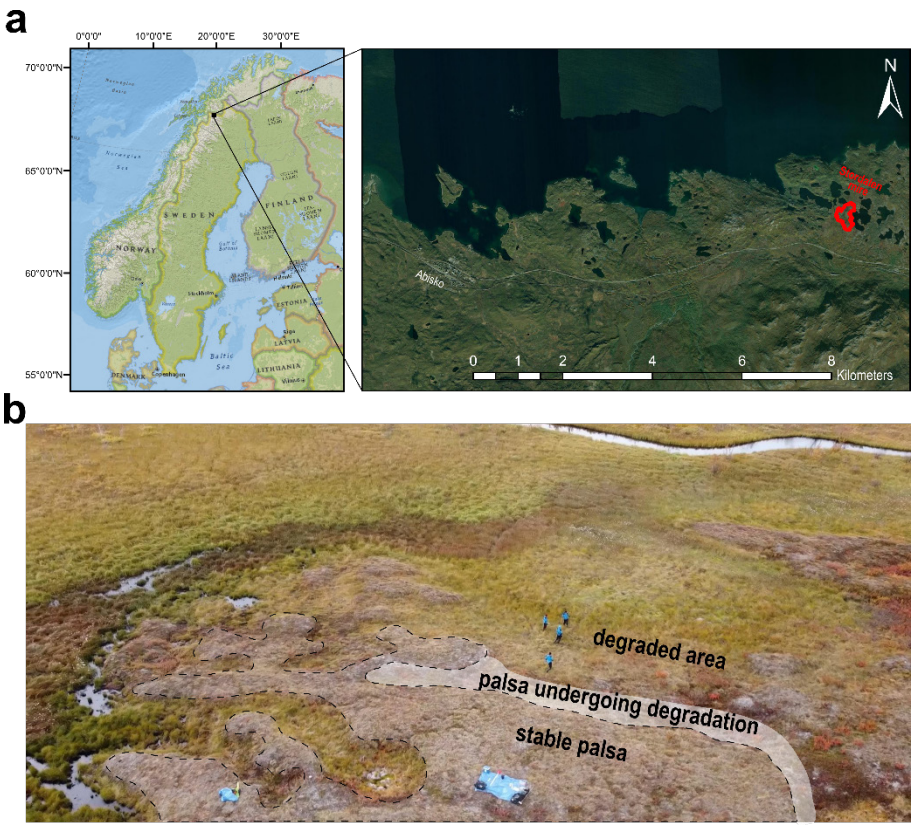

Figure 1 : Location and photograph of the degradation gradient studied. (a) Map of the study site at the Stordalen mire, Abisko Sweden. Map created with ArcMap® 10.8. Basemap sources: National Geographic (© National Geographic et al., 2011) and World Imagery (© Esri and Maxar, 2022). The projected coordinate system is EPSG: 3006. Delineation adapted from Christensen et al. (2004) in red; (b) Illustration of the degradation gradient showing ground subsidence in the field (photo credit: Maxime Thomas)

2.2 Photogrammetric survey

A fieldwork campaign took place between September 14 and October 10, 2021. To obtain data on surface properties, i.e., vegetation, elevation and ground subsidence, we generated a RGB orthomosaic and a digital surface model of the study site by UAS photogrammetry (UAS: DJI MAVIC 2 PRO L1/L2 PPK). The UAS flight took place on September 17th, 2021 at an altitude of 110 m above ground level with a 70% forward overlap and a camera angle of 90°. The perspective centers of the camera were georeferenced with centimeter-level precision by post-processing RINEX data from a GNSS base station located at Abisko Scientific Research Station (swepos.lantmateriet.se; reference station 0ABI) using RTKlib v.2.3.4 software (see Zhang et al., 2019 for post-processing kinematic georeferencing). An orthomosaic and a digital surface model (DSM) have been derived using Agisoft Metashape professional v1.7.5 from 367 images and lead to an initial resolution of 2.66 cm/pixel for the orthomosaic and 5.33 cm/pixel for the DSM.

https://doi.org/10.5194/egusphere-2025-3788
Preprint. Discussion started: 15 August 2025

2.3 Additional historical data

To assess the temporal evolution of the physical degradation in the Stordalen mire, this study incorporates UAS-acquired data from years other than 2021.

(i) We primarily used the 2019 orthomosaic and DSM provided by Siewert and Abisko Scientific Research Station (2020) on the 14 ha extent of the palsa mire (**Fig. 2a**; delineation representing the best compromise between the area covered by our UAS data and the polygon initially drawn by Christensen et al., 2004). These datasets were collected on August 16th, 2019 and have a spatial resolution of ~4 cm for the orthomosaic and ~8 cm for the DSM. For further details on data collection, see de la Barreda-Bautista et al. (2022) and Sjögersten et al. (2023). Together, the 2019 and 2021 datasets provide complementary topographic information and adequate coverage. These were used to develop a classification model for detecting and quantifying the evolution of palsa degradation between 2019 and 2021.

(ii) To capture longer-term trends, we used RGB imagery data spanning from 2014 to 2022, although topographic information is unavailable for this dataset. For this analysis, we selected an extent with consistent data availability (**Fig. 2a**), except for 2020, when data collection was disrupted due to the COVID-19 pandemic. This dataset provides a preliminary estimate of degradation trends from 2014 through 2022. Portions of this data have been previously used in (i) Palace et al. (2018) and Varner et al. (2022) for 2014, (ii) Burke et al. (2019) for 2014 and 2016 and (iii) DelGreco (2018) for the years 2014-2017. Details of these UAS RGB surveys are presented in **Tab. A. 1**.

2.4 Data processing and classification

The various pre-processing operations carried out on the data are detailed below:

(i) Extraction of slopes from DSMs where applicable

(ii) Projection of all data in the EPSG:3006 projected coordinate system (SWEREF99 TM).

(iii) Co-registration of all raster imagery to ensure the best overlap from one year to the next. The 2021 dataset was chosen to be the reference for this study.

(iv) Extraction of the area of interest (**Fig. 2a**).

(v) Resampling of all data at a spatial resolution of 10 cm × 10 cm.

(vi) Removal of the bowl-shape effect from elevation data (DSM), to eliminate systematic distortions or artifacts caused by sensor or data processing errors, ensuring accurate inter-annual comparison (**Fig. A. 2**).

https://doi.org/10.5194/egusphere-2025-3788
Preprint. Discussion started: 15 August 2025

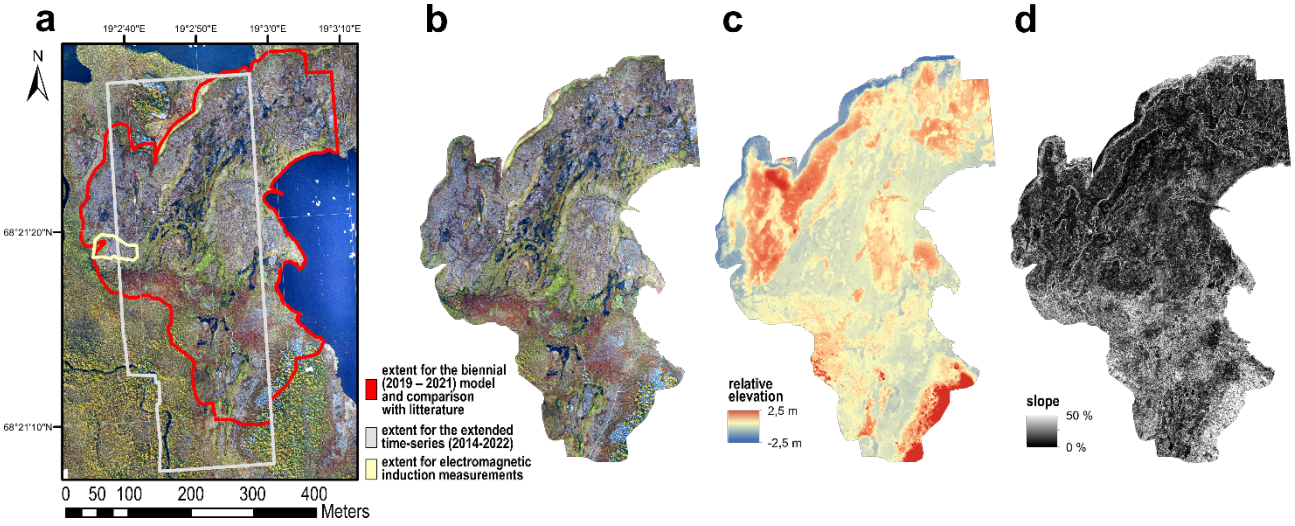

Figure 2: Data processing extents & 2021 input data for classification. (a) Extent of the biennial (2019 – 2021) model (delineation representing the best compromise between the area covered by our UAS data and the polygon drawn by Christensen et al., 2004) in red, extent for the extended time series (2014-2022) in grey and extent used for electrical conductivity measurements in yellow; (b) Orthomosaic composed of red, green and blue bands; (c) Relative elevation after removal of bowl-shape effect (see **Fig. A. 2**); (d) slope extracted from the original digital surface model; the projected coordinate system is EPSG: 3006.

For the biennial (2019 – 2021) model (see **Fig. 2a** for the spatial extent), a supervised classification was implemented in Python and consisted of four static classes that remain unchanged from 2019 to 2021, and three dynamic classes that represent the evolution of the physical degradation between 2019 and 2021. The static classes include (i) stable palsa surfaces, (ii) areas of undergoing or under recent degradation and (iii) degraded areas, which also includes the areas of open water that may not have had permafrost conditions for several decades. It should be noted that, for this model of the evolution of degradation between 2019 and 2021, an 'open water' class is not considered separately due to the fluctuating height of the water table at the time of the photogrammetric survey[2]. An additional (iv) class called 'other' includes outcrops, field equipment, planks, buildings, rocks and trees. The dynamic classes that capture the evolution of the degradation between 2019 and 2021 include (i) the transition from stable palsa in 2019 to palsa undergoing degradation in 2021, (ii) the transition from stable palsa in 2019 to degraded areas in 2021, and (iii) the transition from palsa undergoing degradation in 2019 to degraded areas in 2021 (**Fig. 3**).

Briefly, the classification process involves

(i) Exclusion of relative elevation and slope values from the datasets for each of the two years (2019 and 2021) that deviate from the mean by more than three times the standard deviation.

[2] Degraded permafrost zones and open water zones are interchangeable due to fluctuating water table levels. It is therefore possible that for some patches, open water in 2019 will become degraded in 2021, and vice versa. These two classes have therefore been grouped together.

https://doi.org/10.5194/egusphere-2025-3788
Preprint. Discussion started: 15 August 2025

(ii) Calculation of the difference between 2019 and 2021 relative elevation data to obtain the change in relative elevation between the two years;

(iii) Generation of spatial filters from the original bands using pixel windows of varying sizes (**Tab. 1**):

- Calculation of the mean of pixel values in 3 × 3, 5 × 5 and 7 × 7 moving windows (larger moving windows did not improve the accuracy of the classifications);
- Calculation of the standard deviation of pixel values in 3 × 3, 5 × 5 and 7 × 7 moving windows (larger moving windows did not improve the accuracy of the classifications);
- Application of digital image processing techniques to produce texture attributes based on the gray-level co-occurrence matrix (GLCM; e.g., Hall-Beyer, 2017; Haralick, 1979; Haralick et al., 1973). The calculated texture attributes include entropy, angular second momentum, contrast, homogeneity and the standard deviation of the GLCM, all applied within a 21 × 21 moving window. These texture indices were calculated on all bands, after standardization.

(iv) Classification using a support vector machine (SVM) algorithm. The normalized data served as input for the SVM, with a radial basis function (RBF) as kernel and the gamma parameter set as automatic. The training points were sampled from polygons drawn as representative of each class (by photointerpretation) and spatially distributed across the mire. The distribution of training points for each class is shown in **Tab. A. 2** and the data distributions for the training areas are shown in **Fig. A. 3**.

(v) Refinement of the initial predictions. A set of rules was applied, involving the predicted class and the relative elevation difference between 2019 and 2021. Firstly, if a pixel was predicted as belonging to one of the dynamic classes (i.e., representing the evolution of the degradation between 2019 and 2021) and the corresponding relative elevation difference was positive or null (which therefore does not indicate subsidence), the model re-evaluated the prediction. In this case, the possible identification was limited to one of the static classes that remain unchanged between 2019 and 2021. Conversely, if a pixel was initially assigned to the stable palsa class, and the value of the relative elevation difference was lower than -30 cm (indicating significant subsidence), the model reclassified the pixel by selecting the likeliest identification from the dynamic classes. The reclassification process involved examining the decision scores produced by the model for each sample and selecting the class with the highest decision score from the set of allowed classes.

(vi) Post-processing of the classification output with a majority filter of increasing window sizes, to 11 × 11 pixels, to reduce noise and enhance classification accuracy. Larger filters did not improve the accuracy of the classifications.

Finally, as validation, 1300 points were randomly sampled across the study area and assigned a ground truth class by manual photointerpretation.

https://doi.org/10.5194/egusphere-2025-3788
Preprint. Discussion started: 15 August 2025

Table 1: Input data for the classification model. GLCM = Gray Level Co-Occurrence Matrix.

input data		number of bands			total
		2019	2021	relative elevation change 2019-2021	
original bands (RGB + relative elevation + slope)		5	5	1	11
mean spatial filter in 3 × 3, 5 × 5 and 7 × 7 moving windows		15	15	3	33
standard deviation spatial filter in 3 × 3, 5 × 5 and 7 × 7 moving windows		15	15	3	33
texture	entropy	5	5	1	11
	angular second momentum	5	5	1	11
	contrast	5	5	1	11
	homogeneity	5	5	1	11
	GLCM standard deviation	5	5	1	11
					132

To identify representative classes for the evolution of the degradation between 2019 and 2021, we therefore scanned the different data for the two years of measurement and observed the changes in morphology. An example of the transition from stable palsa in 2019 to degraded permafrost in 2021 is presented in **Fig. 3**.

2.5 Performance evaluation of classification models

We used overall accuracy (**eq. 1**) as a key metric for assessing the quality of the model. Additionally, calculations of precision (**eq. 2**), recall/detection rate (**eq. 3**) and F-score (**eq. 4**) were performed to assess the predictive quality of the different classes.

$$overall\ accuracy\ (OA) = \frac{\sum_i TP_i}{total\ number\ of\ samples} (1)$$

$$Precision_i = \frac{TP_i}{TP_i + FP_i} (2)$$

$$Recall_i = \frac{TP_i}{TP_i + FN_i} (3)$$

$$F - score_i = \frac{2 \times Precision_i \times Recall_i}{Precision_i + Recall_i} (4)$$

Where *i* is the class, *TP* stands for true positive, *FP* stands for false positive, *FN* stands for false negative

https://doi.org/10.5194/egusphere-2025-3788
Preprint. Discussion started: 15 August 2025

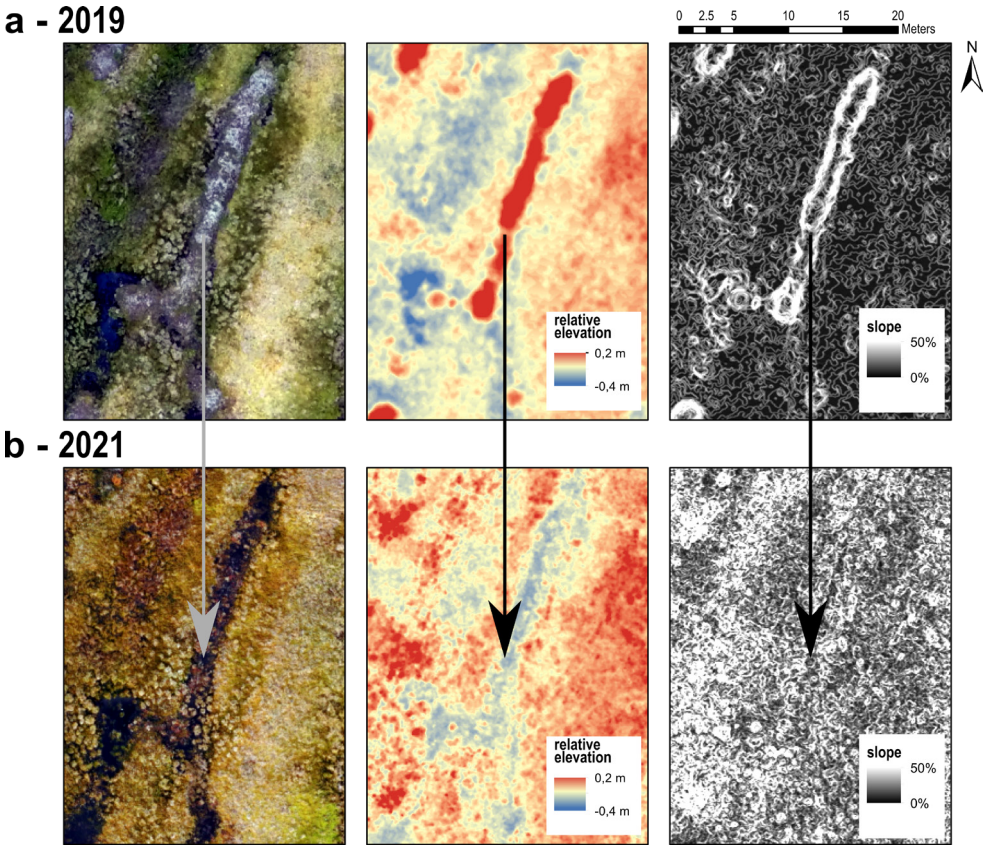

Figure 3: Example of physical degradation between 2019 and 2021 in the Stordalen mire (Abisko, Sweden). (a) 2019 data from Siewert and Abisko Scientific Research Station (2020); (b) Data from this study. From left to right: orthomosaic, relative elevation and slope. Relative elevation data are corrected after removal of the bowl-shape effect; the projected coordinate system is EPSG: 3006.

For the model based on the 2014 – 2022 UAS time series (see **Fig. 2a** for the spatial extent), we used data at a spatial resolution of 5 cm × 5 cm and produced one separate classification for each available year, with the following 4 classes: (i) stable palsa surfaces, (ii) degraded areas, (iii) open water and (iv) the class 'other', which includes outcrops, field equipment, planks, buildings, rocks and trees. From the original spectral bands, we used spatial filters on pixel windows of different sizes: (i) the mean of pixel values in 3 × 3, 5 × 5 and 7 × 7 moving windows, (ii) the standard deviation of pixel values in 3 × 3, 5 × 5 and 7 × 7 moving windows, (iii) the GLCM additional texture features entropy, angular second momentum, contrast, homogeneity and the standard deviation of the GLCM in a 21 × 21 moving window.

A validation dataset of 300 points was randomly sampled over the study area and assigned a ground truth class by manual photointerpretation, for each year of data. The predicted surface areas of each class were estimated by pixel counts. We used confusion matrices to correct for misclassification bias in the output maps (Czaplewski and Catts, 1992; Hay, 1988). In the following, all predicted areas presented were corrected using the confusion matrices.

https://doi.org/10.5194/egusphere-2025-3788
Preprint. Discussion started: 15 August 2025

2.6 Electro-magnetic induction measurements

We hypothesized that the electrical properties of the soil would vary along the degradation gradient. This is because soil electrical conductivity (EC) is influenced by several factors, including soil texture (primarily clay content), water content, salinity, which depends on nutrients, salts, and pH, organic matter type and proportion, soil structure and density, and soil temperature (Doolittle and Brevik, 2014; McNeill, 1980). To investigate these electrical properties, we focused on a 0.2 ha sub-area (**Fig. 2a**) and employed electromagnetic induction (EMI) due to its non-invasive nature, efficiency in covering relatively large areas, and ability to provide continuous conductivity measurements. This approach allows for the identification of spatial heterogeneities in soil properties along the degradation gradient. The instrument used was the EM38, manufactured by Geonics Limited (Ontario, Canada). The EM38 measures soil EC to a depth of 2 m below the sensor, with maximum sensitivity at approximately 30 – 40 cm (Heil and Schmidhalter, 2017). The EC is estimated using the McNeill model (McNeill, 1980), which is widely applied in EMI surveys. This model assumes that the Low Induction Number (LIN) hypothesis is valid, meaning that the instrument response is linearly related to soil EC. For our study site, we verified that the LIN hypothesis holds, as demonstrated by our results. Data collection was conducted by pulling the EM38 on a plastic sledge at a height of a few centimeters above the ground surface. This configuration minimizes soil disturbance while maintaining consistent sensor-to-soil spacing. EMI data and corresponding GNSS positions for 1083 points were recorded using a rugged laptop and a custom-made acquisition program. Continuous EC data were interpolated by kriging of the point values after logarithmic transformation, using a combined nugget and exponential model with a maximum prediction distance of 8 m.

2.7 Use of the classified landscape for scaling up organic carbon stocks

The thematic maps created in this study were used to establish the potential variation in organic carbon stock subsequent to palsa degradation between 2019 and 2021. For each degradation stage (i.e., stable palsa, palsa undergoing degradation and degraded areas), we used the measurements presented in Patzner et al. (2020), which give – for each stage – a characterization of total organic carbon (TOC) content and dithionite/citrate extractable carbon, which is here referred to as mineral-associated organic carbon (MAOC). The study also provides access to the bulk densities and thicknesses associated with the different horizons. Using these data, OC stocks $\left(\frac{kg_{\mathrm{OC}}}{m^2}\right)$ were calculated for each degradation stage (**eq. 5**). This assessment was made for a constant mass of mineral matter for each stage, in order to take subsidence and compaction into account (**Table B. 1**; **eq. B1**). The stock difference between the two years (kg_{OC}) consists in the difference between the stocks in 2019 and 2021, weighted by their respective surface areas for each year (**eq. 6**). These calculations were carried out for TOC and MAOC. The results consist of a TOC or MAOC stock that is made vulnerable annually as a result of palsa degradation. The actual timing of OC loss remains unknown.

$$\text{OC stock}\left(\frac{kg_{\mathrm{OC}}}{m^2}\right)_{j\ \text{degradation stages}} = \sum_{i\ \text{horizons}} \text{bulk density}_i\left(\frac{kg_{\mathrm{soil}}}{m^3}\right) \times \text{thickness}_i\,(m) \times \text{OC content}_i\left(\frac{kg_{\mathrm{OC}}}{kg_{\mathrm{soil}}}\right) \quad (5)$$

https://doi.org/10.5194/egusphere-2025-3788
Preprint. Discussion started: 15 August 2025

$$\Delta \text{ OC stock } (kg_{\text{OC}}) = \sum_{j \text{ degradation stages}} \text{OC stock}_j \left(\frac{kg_{\text{OC}}}{m^2}\right) \times \text{surface area}_{j_{2021}} (m^2) - \sum_{j \text{ degradation stages}} \text{OC stock}_j \left(\frac{kg_{\text{OC}}}{m^2}\right) \times surface\ area_{j_{2019}} (m^2) \quad (6)$$

3 Results and discussion

3.1 Information on topography is critical for detecting permafrost degradation

Several tests have been conducted to determine which parameters provide the best classification results for palsa degradation between 2019 and 2021. The results reveal that topography is a critical factor for achieving optimal model performance. Classification using only RGB imagery data (i.e. 6 spectral bands but no topography information) gives an overall accuracy of 41%. When relative elevation data are added for both years (to reach 8 bands in total), the overall accuracy increases to 67%. The addition of slope data further improves classification, raising the overall accuracy to 76%. The slope additionally doubles the F-scores of both the areas undergoing or under recent degradation and the dynamic classes, which makes it particularly valuable for short-term detection of palsas degradation. When the difference in relative elevation between 2019 and 2021 is included (to reach a total of 11 bands), the overall accuracy reaches 77%. The relative importance of the different bands are shown on **Fig. C. 1a**. For comparison, the use of relative elevation and slope to perform a land cover classification over the Stordalen catchment was also done by Siewert (2018) and resulted in an overall accuracy of 74%. Other studies have shown that relative elevation is an essential parameter for differentiating otherwise so heterogeneous tundra landscapes, e.g., in permafrost-affected soils of the Lena River Delta (Siewert et al., 2016) or in thermokarst-affected terrain types in the periglacial Lena–Anabar coastal lowland (Grosse et al., 2006).

By adding data from the mean spatial filters (3 × 3, 5 × 5 and 7 × 7 window sizes; for a total of 44 bands), the overall accuracy increased to 79%. Incorporating mean spatial filters over larger windows does not increase classification quality. The addition of standard deviation or texture attributes only improves the classification slightly. Adding standard deviation spatial filters improves the overall accuracy to 80%, as does the standard deviation of the GLCM, while the addition of angular second momentum, entropy, contrast or homogeneity increases overall accuracy by only 1%, i.e., to 80.8%. In the following, we will retain only the 'homogeneity' texture parameter, as it enables to reach the highest overall accuracy, while the combination of the texture parameters brings it down to 78%. We believe that GLCM texture attributes contribute little to our model, as topography information already provides a level of morphological information and spatial patterns.

Then, initial predictions were refined using elevation differences and model scores to ensure alignment with domain knowledge (see **section 2.4**). As a result, the overall accuracy improved to 81.3%. As a final post-processing step, the classification result was filtered using windows of increasing size up to 11 × 11 pixels, to reduce noise and enhance classification consistency. The

https://doi.org/10.5194/egusphere-2025-3788
Preprint. Discussion started: 15 August 2025

evolution of the model's performance for each class is shown in **Fig. C. 1b**. These combined operations result in a map with an overall accuracy of 83% (**Fig. 4a**). The best predicted classes are stable palsa, degraded areas and the class 'other' with F-scores of 82%, 89% and 83%, respectively. These are followed by palsa undergoing degradation (35%), the evolution from stable palsa to palsa undergoing degradation (40%), and the evolution from palsa undergoing degradation to degraded areas (30%). The class with the poorest performance is the direct transition from stable palsa to degraded areas, with an F-score of 27% (see confusion matrix in **Tab. 2**). The low F-scores for dynamic classes can be attributed primarily to the fact that these classes have intermediate properties between those of the 'stable', 'undergoing' and 'degraded' classes, making them difficult to differentiate. On the other hand, if we aggregate – for 2019 – the classes 'stable -> undergoing' and 'stable -> degraded' together with the 'stable' class as well as the 'undergoing -> degraded' class with the 'undergoing' class and vice versa for 2021, we obtain overall accuracies of 84% and 86% for 2019 and 2021, respectively. We also obtain significantly improved F-scores, i.e., 49% and 48% for the 'undergoing degradation' class in 2019 and 2021, respectively (see confusion matrices in **Tab. C. 1**; **Tab. C. 2**).

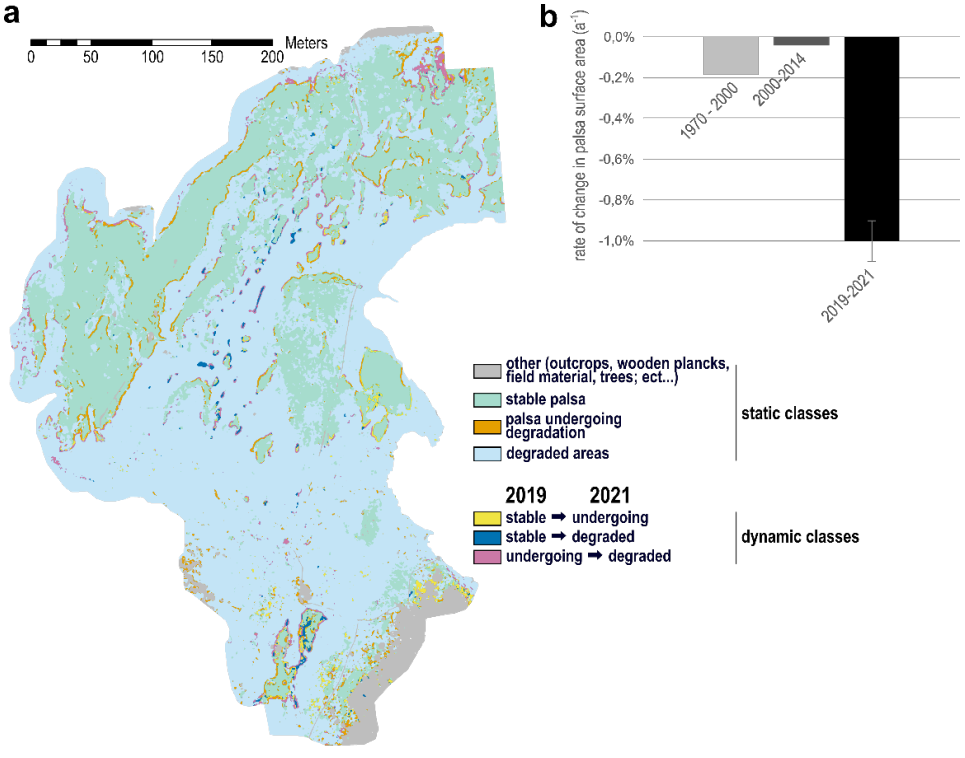

Figure 4: Classification model for the evolution of landscape physical degradation between 2019 and 2021. This model uses 55 bands as input data, namely (i) 11 bands with original data (3 spectral bands, relative elevation and slope for the years 2019 and 2021 as well as the difference in relative elevation between 2019 and 2021) along with (ii) 3 × 11 bands of the mean spatial filter over windows of increasing size, i.e. 3 × 3, 5 × 5 and 7 × 7, and finally (iii) the 11 bands from the texture attribute 'homogeneity'. The classification output was then filtered with a moving window of 11 × 11 pixels. (a) Output landcover map; (b) Rate of change of the stable palsa area for 1970-2000 (Christensen et al., 2004), 2000-2014 (Varner et al., 2022) and 2019 – 2021 (this study). Rates are expressed as a proportion of the entire mire (% reduction per year). The surface area for 2019-2021 are corrected using the confusion matrix.

https://doi.org/10.5194/egusphere-2025-3788
Preprint. Discussion started: 15 August 2025

Table 2: Confusion matrix for the classification model & precision, recall and F-score for each cover class. This model uses 55 bands as input data, namely (i) 11 bands with original data (3 spectral bands, relative elevation and slope for the years 2019 and 2021 as well as the difference in relative elevation between 2019 and 2021) along with (ii) 3 × 11 bands with spatial filters (mean & standard deviation) over windows of increasing size, i.e. 3 × 3, 5 × 5 and 7 × 7, and finally (iii) the 11 bands from the texture attribute 'homogeneity'. The classification output was then filtered with a moving window of 11 × 11 pixels.

		predicted										
		other	stable palsa	undergoing degradation	degraded areas	stable → undergoing	stable → degraded	undergoing → degraded		Precision	Recall	F-score
Actual	other	**55**	0	3	7	1	0	0	66	83%	83%	83%
	stable palsa	2	**294**	6	25	0	1	2	330	89%	76%	82%
	undergoing degradation	1	22	**18**	22	1	1	2	67	27%	49%	35%
	degraded areas	8	65	10	**702**	1	1	12	799	88%	91%	89%
	stable → undergoing	0	1	0	1	**3**	1	1	7	43%	38%	40%
	stable → degraded	0	2	0	3	0	**2**	0	7	29%	25%	27%
	undergoing → degraded	0	1	0	10	2	2	**7**	22	32%	29%	30%
		66	385	37	770	8	8	24	1298			

3.2 Palsa degradation accelerates in the Stordalen mire and can be tracked over two years of data

When we compare the rate of palsa degradation for the period 2019 – 2021 in Stordalen with past studies, we observe a clear acceleration. More specifically, the study by Christensen et al. (2004) reported a rate of disappearance of stable palsa zones averaging 0.2%·a^{-1} (relative to the total land cover area, i.e., degradation rate as a proportion of the entire mire) between 1970 and 2000, based on vegetation distribution from infrared aerial photographs. Varner et al. (2022) estimated an average palsa loss of 0.04%·a^{-1} between 2000 and 2014 (the 2014 dataset being based on 2014 WorldView 2 satellite imagery), suggesting a deceleration in palsa loss after 2014 relative to the earlier assessment at Stordalen (i.e., 1970 – 2000; Christensen et al., 2004). In this study, we revisit these estimates for the period 2019 – 2021 and we obtain a decrease in palsa surface area of 0.9%·a^{-1} to 1.1%·a^{-1} (**Fig. 4b**). This suggests that the rate of permafrost degradation in the Stordalen mire is approximately 5 times faster in recent years compared to previous periods. Besides, for Stordalen and two other mires in the same valley, de la Barreda-Bautista et al. (2022) mapped lateral erosion of 3.1 – 9.3 m between 1960 and 2018 with slower rates of 0.03 – 0.12 m·a^{-1} between 1960 and 2002 and thereafter and acceleration with the highest rates between 2002 and 2018 with 0.18 – 0.32 m·a^{-1}. This confirms the increasing rate of palsa loss in the mire.

In Turetsky et al. (2020), the rate of degradation from permafrost peatlands into either active thaw lakes or wetlands was assessed to be 0.2%·a^{-1} (relative to the total land cover area). Yet this is the only study that attempts - on an Arctic scale - to estimate the changes in greenhouse gas emissions (via cumulative net ecosystem carbon balance estimates) caused by the

https://doi.org/10.5194/egusphere-2025-3788
Preprint. Discussion started: 15 August 2025

development of these thermokarst landscapes. According to the published literature and from this study, however, a permafrost peatlands degradation rate of 0.2%·a^{-1} appears to be a fairly conservative estimate in comparison with 0.58%·a^{-1} from 2000 to 2015 (of plateau to wetland conversion in the Northwest Territories, Canada; Chasmer and Hopkinson, 2017), ~0.7%·a^{-1} between 2008 and 2018 (of formation of thermokarst depressions in central Alaska; Rodenhizer et al., 2022) and 0.9%·a^{-1} to 1.1%·a^{-1} (this study).

If we base calculations on the extent of the palsas alone (i.e., palsa degradation rate as a proportion of the initial palsa areal extent), our study shows a decrease of 3.5%·a^{-1}, which compares with 0.6%·a^{-1} - 1.2%·a^{-1} (from the 1950s to the 2010s, with the largest lateral change rates observed after 2000) study by Borge et al. (2017) in northern Norway and average rates of 0.71%·a^{-1} to 1.25%·a^{-1} between 1955 and 2016 in the Vissátvuopmi palsa complex in Sweden (Olvmo et al., 2020). Average palsa areal losses of 0.5%·a^{-1} to 2.8%·a^{-1} can also be noted in the eastern Selwyn/western Mackenzie Mountains in Canada (Mamet et al., 2017), with the decline following a non-linear pattern. All of these studies suggest that palsa degradation is likely to continue, with a non-linear decline, probably at a higher rate than today (Borge et al., 2017; Mamet et al., 2017; Olvmo et al., 2020; Renette et al., 2024). Recent modeling studies besides state that environmental or climate spaces for palsas and peat plateaus are threatened by imminent loss at a circumpolar scale (Fewster et al., 2022; Leppiniemi et al., 2023).

Such assessments of palsa loss rates and development of lowland thermokarst are critical prerequisites for predictive models of permafrost carbon balance from such landscapes. In this study and from available literature, we show that there is still much uncertainty surrounding these estimates beyond local scales, leading to a potential mis-evaluation of the impact of lowland thermokarst on the permafrost carbon balance. From this study, we are confident in asserting that with only biennial data from photogrammetric surveys, we can trace the evolution of palsa degradation. In order to monitor this state of degradation, the method proposed here could be extended to cover a large number of study sites without requiring extensive computing capacity.

3.3 Palsa degradation means higher levels of humidity

Using the classification model from the broader temporal view (2014 – 2022; **Fig. 5**), we observe a trend towards an increase in the area of fully thawed and inundated fen. The surface area of stable palsa decreased at an average rate of 2.2 ± 1.1 %·a^{-1} between 2014 and 2022 (95% confidence interval (CI); R^2 = 0.79). The degraded areas (fen) have in turn increased at an average rate of 2.2 ± 1.5%·a^{-1} (95% CI; R^2 = 0.69). Finally, we note that the fraction of the open water class has more than doubled in size between 2014 and 2022, with an average increase of 0.3 ± 0.4%·a^{-1} (95 % CI; R^2 = 0.31). These rates of surface area change appear to be higher, but remain within the same order of magnitude as the biennial model (2019-2021). It should be noted that the spatial extent is not identical to that presented in section 3.2 (see **Fig. 2a**). Furthermore, the model from the 2014 – 2022 UAS time series does not use terrain morphology data (relative elevation and slope) for classification. As a result, its quality indicators (**Fig. 5a**) are weaker than for the biennial model (**Tab. 2**), for which topography data were used. We believe, however, that it can provide indication of trends, and has the advantage of enabling tracking of the 'open water' class surface area, which is not possible with the biennial model.

https://doi.org/10.5194/egusphere-2025-3788
Preprint. Discussion started: 15 August 2025

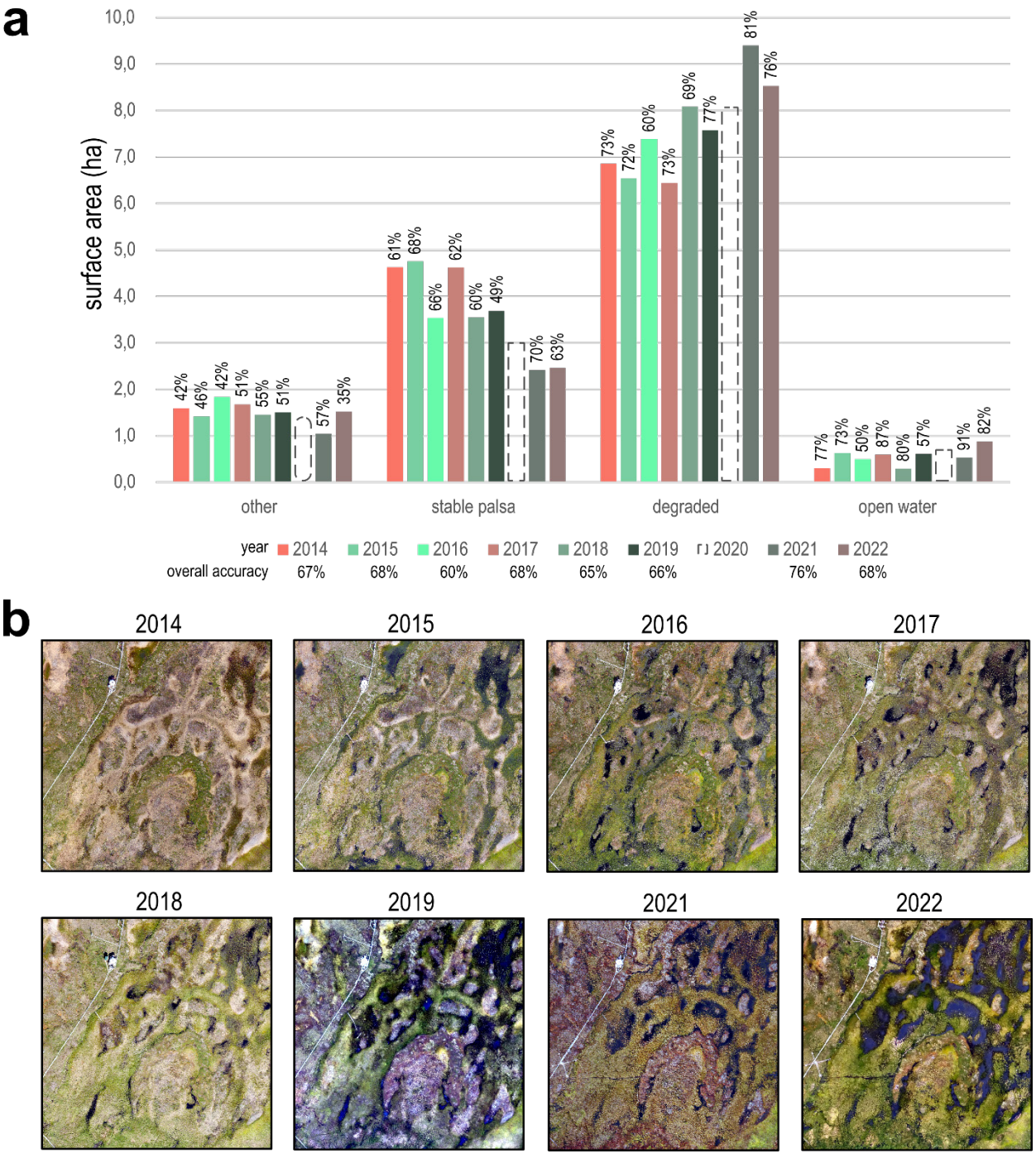

Figure 5: Classification model results based on imagery data spanning from 2014 to 2022. (a) Evolution of the surface areas (corrected using the confusion matrix) of the 4 classes, i.e. (i) stable palsa, (ii) degraded areas (fully thawed fen), (iii) open water and (iv) the class 'other', which includes field equipment, planks, buildings, rocks and trees. Bar colors represent years. Percentages above the bars represent the F-score. The overall accuracy of each of the annual classifications is also shown. (b) Extract (clip) of original data for each available year.

https://doi.org/10.5194/egusphere-2025-3788
Preprint. Discussion started: 15 August 2025

Electrical conductivity (EC) data obtained from electromagnetic induction (EMI) range from 4.1 to 7.8 mS/m over the survey area (**Fig. 6a**) and are well aligned with relative elevation and the predicted degradation classes (**Fig. 6b-e**). This range of values allows for the use of the Low Induction Number (LIN) hypothesis, enabling the estimation of soil EC from the quad-phase component of the measured field, as the LIN assumption is met (McNeill, 1980). The EC values are relatively low, reflecting the absence or minimal presence of clay and low salinity. This observation aligns with the hydrological regime of the area, where surface water is primarily rain-fed, with limited inputs from mineralized groundwater or subsurface flow (e.g., Henrion et al., 2024). The central part of the area exhibits the lowest EC values, which correspond to the highest elevation and stable palsa area. This pattern is consistent with the hydrological gradient, as higher elevations typically exhibit better drainage, reducing water content and, consequently, EC. Electrical conductivity patterns also align with the distribution of vegetation types, as shown in the RGB orthophoto (**Fig. 6d**). Notably, areas with more developed vegetation correspond to areas with higher EC values, likely due to increased water and nutrient availability in these zones, which supports greater plant growth. A clear linear relationship is observed between EC and relative elevation ($R^2 = 51\%$; **Fig. 6e**), further emphasizing the influence of micro-topography on soil hydrology and conductivity. Significant differences in EC are also observed between the different degradation classes (p-values from Kruskal-Wallis test $< 10^{-3}$; **Fig. 6f**). Degraded areas consistently exhibit higher EC values compared to stable palsa, further supporting the role of water content as a key factor driving changes in EC. Since high EC is indicative of increased water content (assuming other factors such as clay content, salinity, and soil mineralogy remain constant), these data suggest that palsa degradation induces a net increase in soil moisture. This process is likely to shift the soil environment toward more anaerobic conditions, reducing organic matter geochemical stability (e.g., Monhonval et al., 2023; Patzner et al., 2020), but also favoring processes such as methanogenesis (e.g., Varner et al., 2022), which could have significant implications for greenhouse gas emissions.

https://doi.org/10.5194/egusphere-2025-3788
Preprint. Discussion started: 15 August 2025

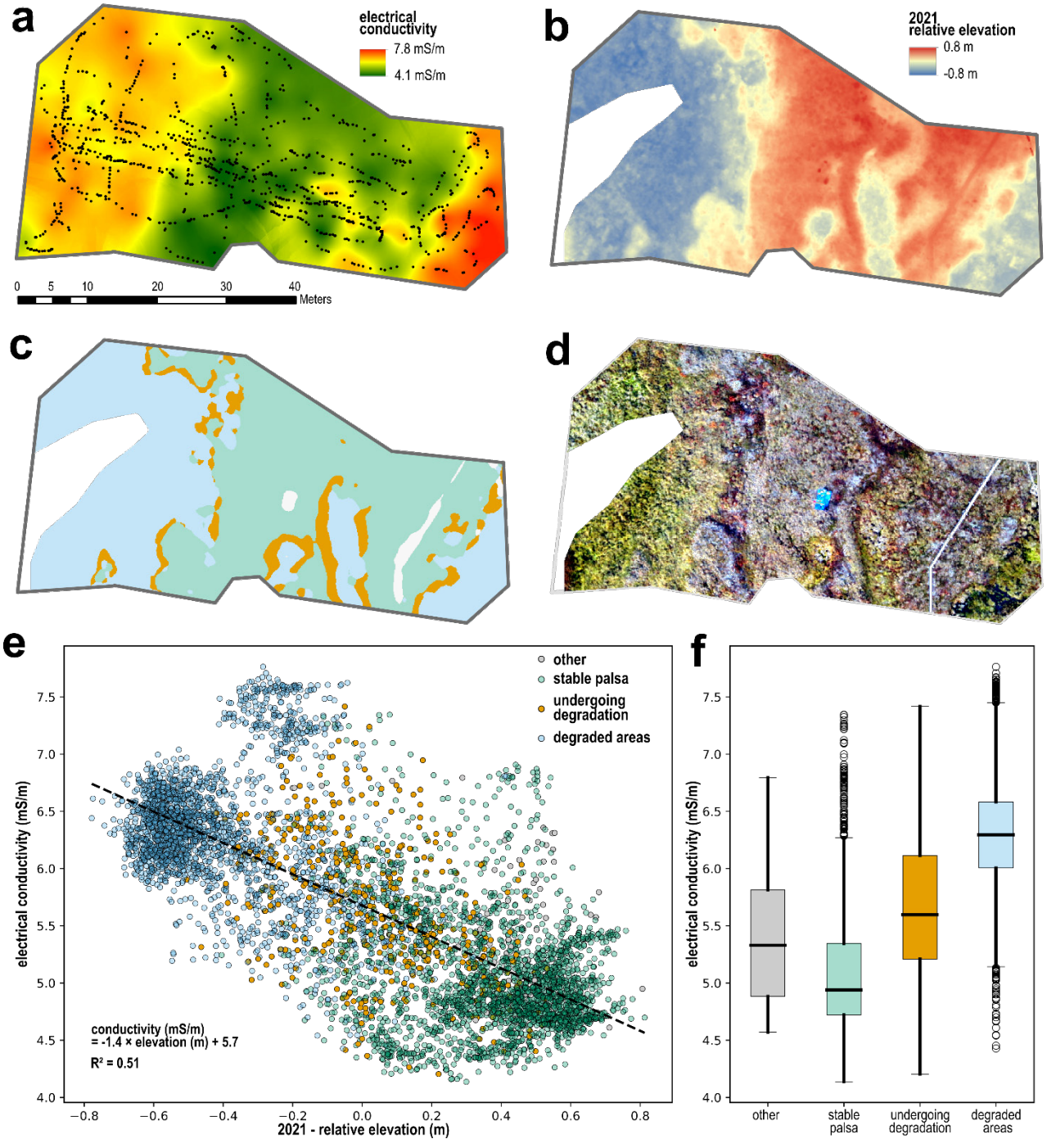

Figure 6: Evolution of electrical conductivity data and comparison with the results of the biennial classification model (between 2019 and 2021). (a) Continuous map of electrical conductivity obtained by simple kriging of point data; (b) Relative elevation data corrected by removal of the bowl-shape effect; (c) Classification model results for 2021 (see **Fig. 4b** for the entire model); (d) RGB imagery data for 2021; (e) Linear regression between electrical conductivity and relative elevation for the different classes; (f) Boxplots of the evolution of electrical conductivity as a function of the class. Data processing extent as in **Fig. 2a**. Color code as in **Fig. 4**.

https://doi.org/10.5194/egusphere-2025-3788
Preprint. Discussion started: 15 August 2025

425

3.4 Implications of palsa degradation for both organic carbon stability and greenhouse gas emissions

The land-cover is generally a very important predictor for both the distribution of organic carbon and GHG emissions (e.g., Siewert, 2018; Varner et al., 2022). For first order estimates of the evolution of OC stocks or GHG emissions in Stordalen, we used a space for time approach using the thematic maps developed in this study (**section 3.2**). To this end, Patzner et al. (2020) showed a drop in the concentration of TOC and MAOC along the degradation gradient in the Stordalen mire. Using estimates of the surface area degraded between 2019 and 2021, we calculated that – for the 14 ha of this study site and for a palsa depth of 23 cm – palsa degradation results in 24 metric tons of TOC becoming vulnerable to decomposition, including 6 metric tons of MAOC (calculations details are available in **Tab. B. 1** – **Tab. B. 2**). This corresponds to a balance of -1.6%·a^{-1} relative to the TOC stock in 2019 and -3.3%·a^{-1} relative to the MAOC stock in 2019. They consist of TOC or MAOC stocks that are made vulnerable annually as a result of palsa degradation and represent first order estimates. The actual proportion and timing of OC export or GHG emissions remain unknown. With regard to GHG emissions, Sjögersten et al. (2023) showed a substantial increase in methane emissions from stable palsa surfaces plant communities to degrading and inundated plant communities highlighting the importance of not only the degree of degradation, but also the vegetation community composition dictating magnitudinal differences in CH_4 emissions. Varner et al. (2022) showed that the net radiative forcing of the Stordalen mire shifted from a slightly negative value before 2000 to a strongly positive value after that date, and increased again in 2014. As a result of accelerated degradation (**section 3.2**), we can expect the radiative forcing to become even more positive through increased CH_4 emissions, as the mire turns wetter (**section 3.3**). Likewise, Łakomiec et al. (2021) measured field-scale CH_4 emissions at Stordalen of 2.7 ± 0.5 and 8.2 ± 1.5 g-C·m^{-2}·a^{-1} (mean annual emissions) for the palsa and thawing surfaces, respectively. With the palsa degradation rates calculated in this study, this would mean that the average annual emissions would increase from ~ 7.1 g-C·m^{-2}·a^{-1} in 2019 to ~ 7.3 g-C·m^{-2}·a^{-1} in 2021 for the entire mire, i.e., an increase of ~1.3%·a^{-1}.

3.5 From local to Arctic scale

Predicting the response of permafrost terrains to climate change and disturbances beyond local scales is extremely difficult (Nicolsky et al., 2017). Discrepancies very often exist between circumpolar-scale and local scale models. This is for instance the case for total organic carbon maps between local estimates (e.g., Fuchs et al., 2015; Palmtag et al., 2015; Siewert, 2018) that show much lower or higher results than circumpolar estimates (Hugelius et al., 2013, 2014). The large-scale estimates used in global or regional models fail to reflect the heterogeneity observed in this typical Arctic environment, where soil properties are highly variable on scales of a few tens of centimeters and often defined by landforms and their degradation trajectory (Siewert et al., 2021), as is the case in Abisko and in many other Arctic environments. Yet, the importance of wetlands for organic carbon stocks at the arctic scale has long been pointed out (e.g., Siewert, 2018). When the temporal evolution component is added, these global estimates are even more difficult to achieve. In the present study, we saw that the parameters of relative elevation and slope (and their evolution) were key components in detecting the formation of thermokarst

https://doi.org/10.5194/egusphere-2025-3788
Preprint. Discussion started: 15 August 2025

in lowland peat rich landscapes. However, digital elevation models across the Arctic are generated from multi-annual data, e.g. 15 years for ArcticDEM (Porter et al., 2023). Although efforts are being made to generate annual elevation models e.g. for the Greenland Ice Sheet (Winstrup et al., 2024), such circumpolar-scale data are not yet available. Still, similar studies could be conducted on multiple thermokarst landscapes across the arctic and at different latitudes. This approach would provide valuable insight into the variability of degradation rates, which could then be included in models such as those used in Turetsky et al. (2020) or Hugelius et al. (2020). A promising approach is the use of InSAR to detect thermokarst and quantify permafrost degradation as well as resulting GHG emissions (van Huissteden et al., 2021; Sjögersten et al., 2023; Valman et al., 2024), but de la Barreda-Bautista et al. (2022) highlight the relevance to use UAS data to ground truth such efforts. A further avenue for monitoring the development of thermokarst landscapes on a circumpolar scale would be to measure the evolution of soil moisture over time. In that respect, drone-borne ground-penetrating radar (GPR) has demonstrated significant potential for high-resolution mapping of soil electrical conductivity and soil moisture (Wu et al., 2019; Wu and Lambot, 2022). Unlike other proximal or remote sensing sensors, which are limited to surface property characterization, GPR provides depth-resolved information, enabling the detection of subsurface changes linked to permafrost degradation, such as increases in soil moisture and ground subsidence.

4 Conclusions

We investigated a gradient of lowland thermokarst development at Stordalen mire, Abisko, Sweden, from well-drained stable palsas to inundated fens, which have undergone ground subsidence. We have conducted an evaluation of palsa degradation through time based on photogrammetric surveys providing access to RGB imagery and topography (relative elevation and slope) data between 2019 and 2021, and a coarser evaluation with RGB imagery only between 2014 and 2022. Our results lead to the following conclusions:

(1) Topography is a critical parameter for determining the evolution of palsa degradation. Including relative elevation and slope data increases the overall classification accuracy from 41% to 77%, highlighting the value of topographic information for identifying palsa degradation. Slope further enables better detection of the early stages of degradation.

(2) We observe a clear acceleration of degradation in Stordalen between 2019 and 2021, with a decrease in stable palsa area of 0.9%·a^{-1} – 1.1%·a^{-1} compared to previous studies for 1970 – 2000 (~0.2%·a^{-1}) and 2000 – 2014 (~0.04%·a^{-1}).

(3) Our coarser evaluation based solely on RGB imagery leads to higher rates though of the same order of magnitude for the period 2014 – 2022 (i.e., 2.2 ± 1.1 %·a^{-1}), and likewise demonstrates a twofold increase in the surfaces of open water. Electromagnetic induction data also supports the increase in soil moisture as palsas degrade, which is likely to alter the soil environment towards more anaerobic conditions.

(4) By combining the rates of palsa degradation from this study with existing data on carbon concentration, stability and release from the study site, we calculated that palsa degradation at Stordalen might lead to a pool of 12 metric tons of organic carbon exposed annually for the topsoil (23 cm depth), of which ~25% is mineral-interacting organic carbon.

https://doi.org/10.5194/egusphere-2025-3788
Preprint. Discussion started: 15 August 2025

Likewise, average annual emissions would increase from ~ 7.1 g-C·m^{-2}·a^{-1} in 2019 to ~ 7.3 g-C·m^{-2}·a^{-1} in 2021 for the entire mire, i.e., an increase of ~1.3%·a^{-1}.

(5) Scaling this approach to the circumpolar Arctic poses a major challenge. Small topographic changes associated with thermokarst development are not captured by satellite images, making the detection of this process challenging. Applying the methodology developed in this study to cover a large number of study sites would allow to assess the spatial variability of degradation rates and thus serve as an input for net ecosystem carbon balance models.

https://doi.org/10.5194/egusphere-2025-3788
Preprint. Discussion started: 15 August 2025

Appendix A | Additional methodological information

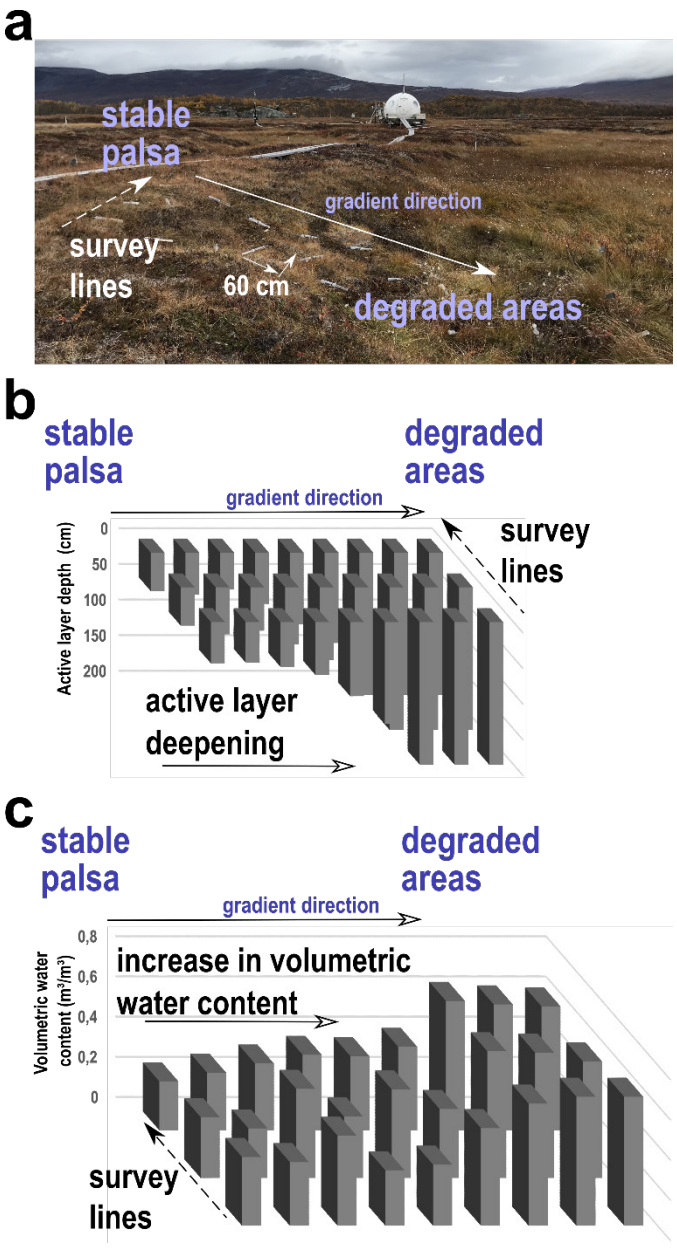

Figure A. 1: Conceptual model and illustration of the permafrost degradation gradient at the Stordalen Mire. (a) measuring grid along the gradient (photo: S. Opfergelt; Sept 30, 2021) where point-to-point distance is indicated for scale; (b) evolution of active layer depth along the gradient; (c) evolution of the volumetric water content along the gradient

https://doi.org/10.5194/egusphere-2025-3788
Preprint. Discussion started: 15 August 2025

Table A. 1: Summary of the different unoccupied aircraft system (UAS) data used in this study. agl = above ground level

year	day of survey	UAS	Sensor	Flight altitude	Original resolution (m)	refs
2014	July 11	Robota Triton XL	Panasonic Lumix-GM1	70 m agl	0,03 × 0,03	dataset: Palace et al. (2019) previously used in Burke et al. (2019); DelGreco (2018); Palace et al. (2018); Varner et al. (2022)
2015	July 11	Robota Triton XL	Panasonic Lumix-GM1	70 m agl	0,03 × 0,03	dataset: Palace et al. (2022a) previously used in DelGreco (2018)
2016	July 12	Robota Triton XL	Panasonic Lumix-GM1	70 m agl	0,03 × 0,03	dataset: Palace et al. (2022b) previously used in Burke et al. (2019); DelGreco (2018)
2017	July 25	Robota Triton XL	Panasonic Lumix-GM1	70 m agl	0,03 × 0,03	dataset: DelGreco et al. (2022) previously used in DelGreco (2018)
2018	July 28	Robota Triton XL	Panasonic Lumix-GM1	70 m agl	0,02 × 0,02	dataset: Palace et al. (2025a)
2019	August 16	Sensefly Ebee	Canon G9x	98 m agl	0,04 × 0,04	dataset: (Siewert and Abisko Scientific Research Station, 2020)
2021	September 17	DJI MAVIC 2 PRO L1/L2 PPK	1” CMOS, 20 MP Lens: FOV: about 77° (35 mm) Format Equivalent: 28 mm Aperture: f/2.8–f/11	110 m agl	0,05 × 0,05	dataset: Thomas et al. (2025)
2022	July 15	Phantom 4 RTK+	1" CMOS, 20 MP Lens: FOV: 84° (35 mm) Format Equivalent: 24 mm Aperture: f/2.8–f/11	100 m agl	0,06 × 0,06	dataset: Palace et al. (2025b) first time use in this study

https://doi.org/10.5194/egusphere-2025-3788
Preprint. Discussion started: 15 August 2025

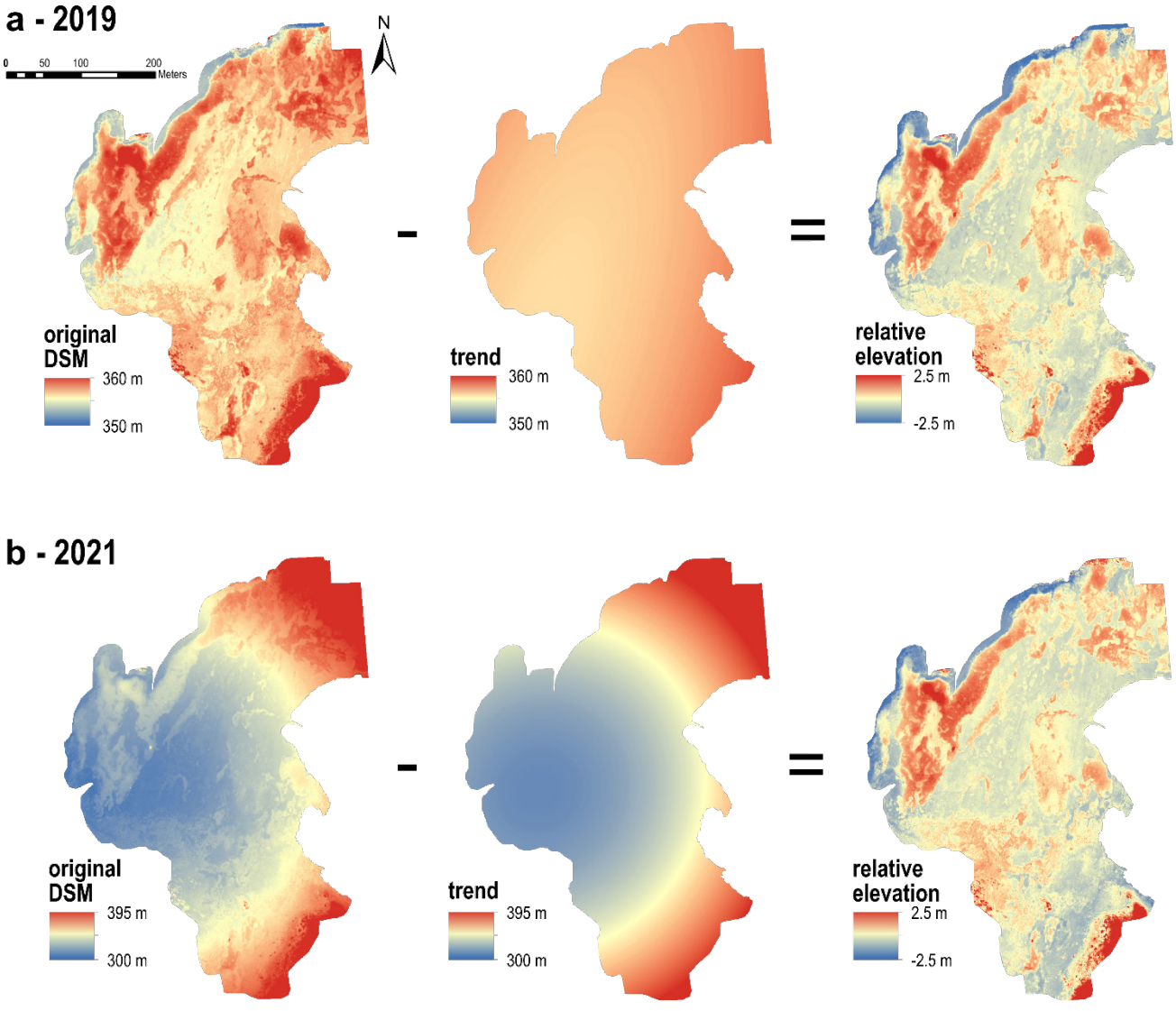

Figure A. 2: Removing of the bowl-shape effect from elevation data (DSM) for (a) 2019 and (b) 2021. The processing involves (i) extraction of the original elevation band on a regular 5 m x 5 m grid; (ii) on this grid, exclusion of the data that diverge by more than 3 times the standard deviation, and calculation of the second-order trend from those data that from the original elevation data; (iii) calculation of residuals by subtraction of the 2nd-order trend from the original data. The result represents the relative elevation data (corrected DSM)

https://doi.org/10.5194/egusphere-2025-3788
Preprint. Discussion started: 15 August 2025

Table A. 2: Distribution of training points for each class.

Class	Number of points for training
other (outcrops, wooden plancks, field material, rocks, etc.)	1752
stable palsa	1995
palsa undergoing degradation	1470
degraded areas	1984
stable palsa → palsa undergoing degradation	1069
stable palsa → degraded areas	1159
palsa undergoing degradation → degraded areas	1075

https://doi.org/10.5194/egusphere-2025-3788
Preprint. Discussion started: 15 August 2025

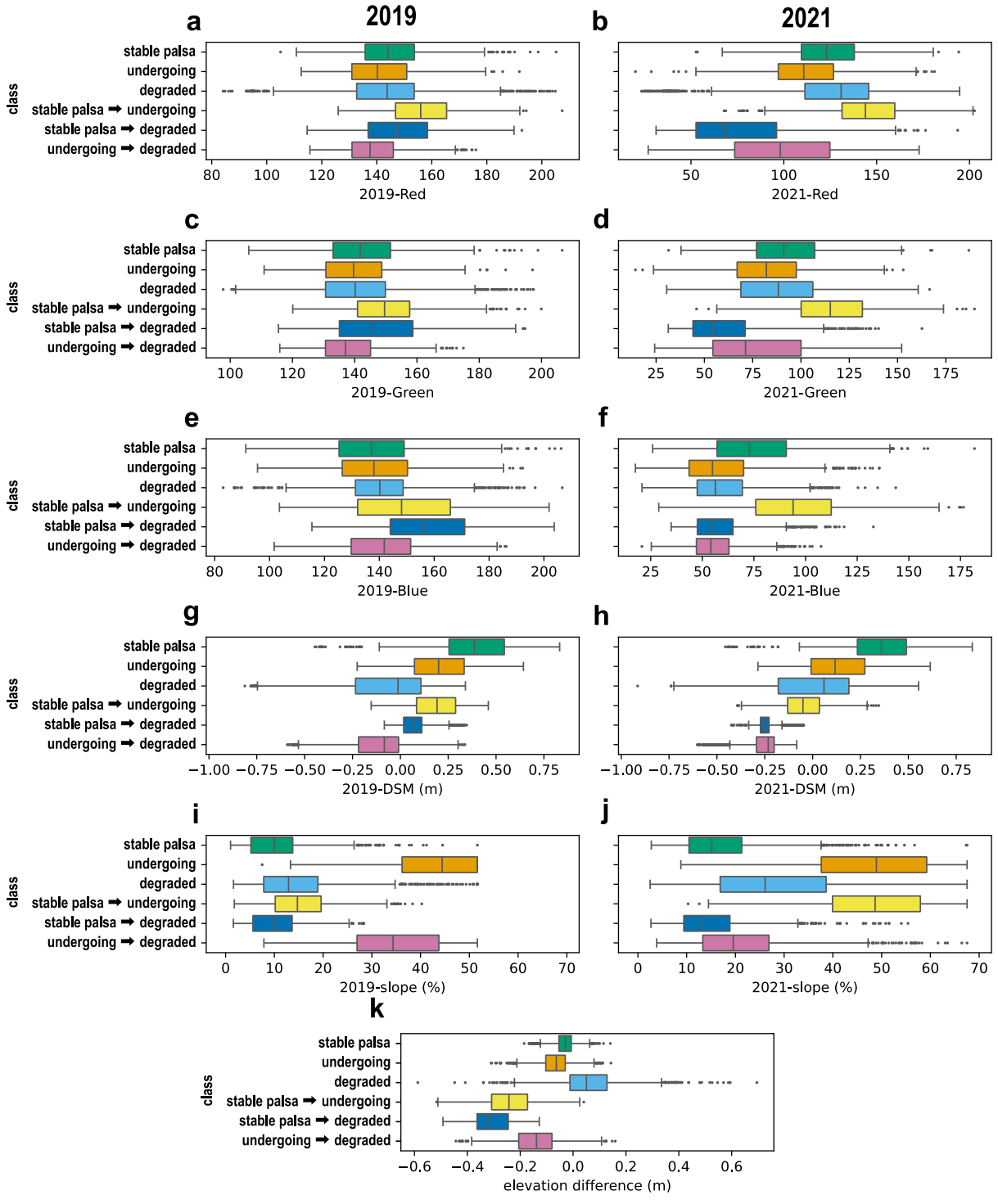

Figure A. 3: Distribution of the selected input data values across the training areas of the classification model, namely (a-b) red color, (c-d) green color, (e-f) blue color, (g-h) relative elevation data corrected by removal of the bowl-shape effect, (i-j) slope values derived from the original DSM and (k) the difference in relative between 2019 and 2021. DSM = digital surface model. Color code as in **Fig. 4**.

https://doi.org/10.5194/egusphere-2025-3788
Preprint. Discussion started: 15 August 2025

Appendix B | Tables for scaling up organic carbon stocks

Table B. 1: Method for scaling up organic carbon stocks from the use of the classified landscape. TOC = total organic carbon; MAOC = mineral-associated organic carbon. Thickness, bulk density, TOC and MAOC data from Patzner et al. (2020). OH = organic horizon; TZ = transition zone; MH = mineral horizon.

degradation stage	Horizon	Thickness (m)	Thickness (m)	bulk density (kg/m³)	Total organic carbon (TOC) ($\%_{wt}$)	Mineral-associated organic carbon (MAOC) ($\%_{wt}$)	Mass of soil/sediment (kg/m²)						Stock of TOC (kg/m²)	Stock of MAOC (kg/m²)
							total		organic		mineral			
stable palsa	OH	0,04	0,23	30	42,4%	0,1%	1	90	1	18	0	72	0,51	0,00
		0,05		30	42,3%	0,2%	2		1		0		0,63	0,00
	TZ	0,01		80	31,2%	3,1%	1		0		0		0,25	0,02
		0,03		80	35,5%	5,3%	2		1		1		0,85	0,13
	MH	0,04		840	13,6%	2,7%	34		8		26		4,57	0,92
		0,06		840	7,3%	1,4%	50		6		44		3,66	0,68
undergoing degradation	OH	0,07	0,13	80	33,3%	1,6%	6	82	3	10	2	72	1,87	0,09
	TZ	0,05		1290	5,8%	2,3%	65		6		58		3,71	1,46
	MH	0,01		1740	0,8%	0,0%	12		0		11		0,10	0,00
degraded areas	OH	0,04	0,08	210	23,5%	0,0%	8	77	3	5	5	72	1,97	0,00
	TZ	0,03		1970	1,6%	0,0%	59		2		57		0,96	0,00
	MH	0,01		1720	0,4%	0,0%	9		0		9		0,03	0,00

$$\text{mineral matter stock } \left(\frac{kg_{mineral\ matter}}{m^2}\right)_i = \left(\text{bulk density}_i \left(\frac{kg_{soil}}{m^3}\right) \times \text{thickness}_i\,(m)\right) - \left(\left(\text{bulk density}_i \left(\frac{kg_{soil}}{m^3}\right) \times \text{thickness}_i\,(m) \times \text{OC content}_i \left(\frac{kg_{OC}}{kg_{soil}}\right)\right) \times 1{,}724 \left(\frac{kg_{organic\ matter}}{kg_{OC}}\right)\right) \quad (B1)$$

https://doi.org/10.5194/egusphere-2025-3788
Preprint. Discussion started: 15 August 2025

Table B. 2: Results of scaling up organic carbon stocks from the use of the classified landscape. TOC = total organic carbon; MAOC = mineral-associated organic carbon. Surfaces in 2019 and 2021 from **Fig. 4**.

degradation stage	Thickness (m)	surface 2019 (ha)	Stock of TOC 2019 (ton)			Stock of MAOC 2019 (ton)			surface 2021 (ha)	Stock of TOC 2021 (ton)			Stock of MAOC 2021 (ton)		
stable palsa	0,04	4,50	23	471	748	0	79	87	4,18	21	438	724	0	74	81
	0,05		29			0				27			0		
	0,01		11			1				10			1		
	0,03		38			6				36			5		
	0,04		206			41				191			38		
	0,06		165			31				153			29		
undergoing degradation	0,07	0,49	9	28		0	8		0,47	9	27		0	7	
	0,05		18			7				17			7		
	0,01		0			0				0			0		
degraded areas	0,04	8,41	166	249		0	0		8,74	172	259		0	0	
	0,03		81			0				84			0		
	0,01		3			0				3			0		

https://doi.org/10.5194/egusphere-2025-3788
Preprint. Discussion started: 15 August 2025

Appendix C | Additional results

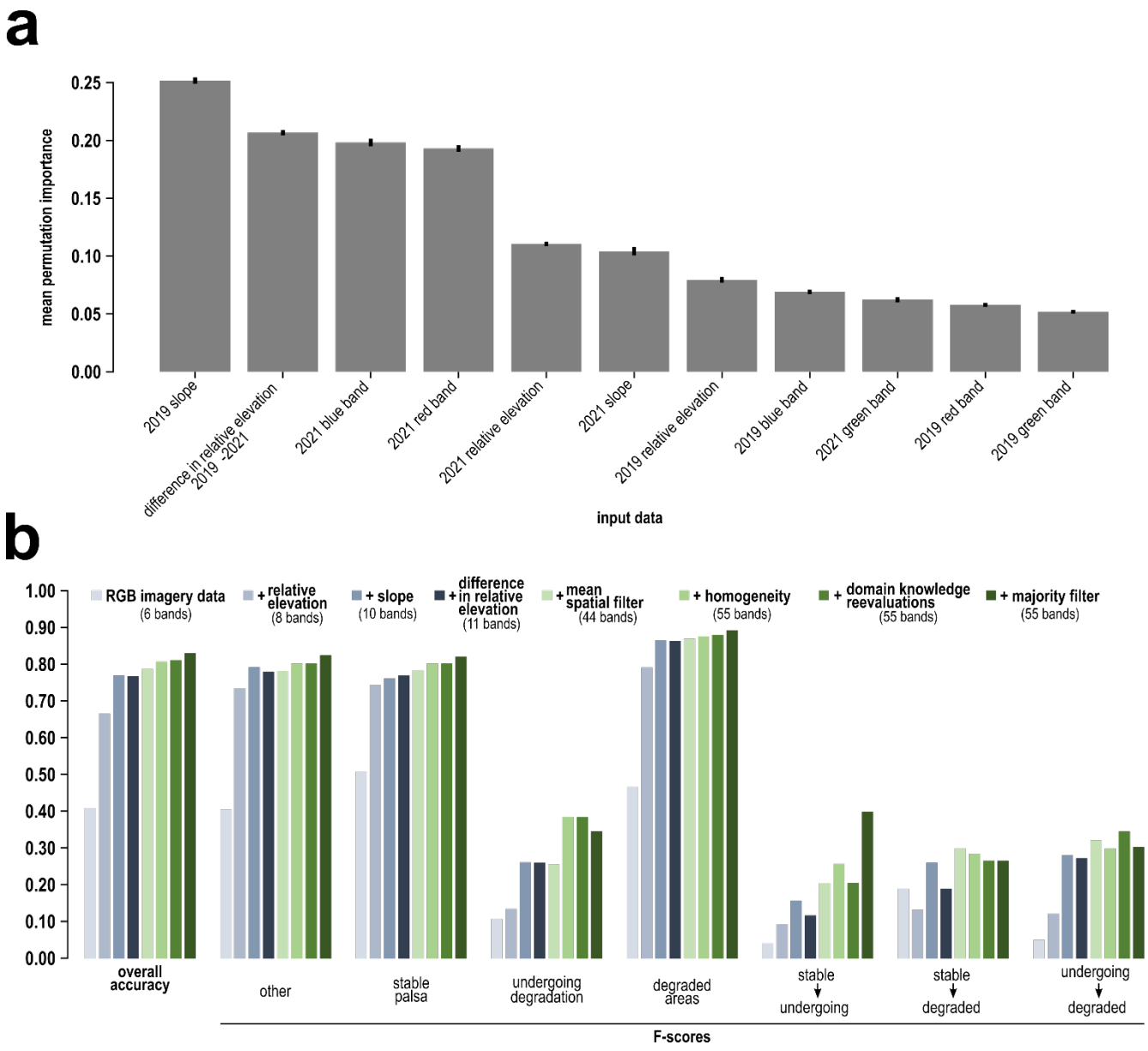

Figure C. 1: Performance evaluation of the biennial (2019 – 2021) model. (a) Mean permutation importance of each input data in the model, measured as the decrease in accuracy when the input data values are randomly shuffled. The error bars indicate the standard deviation of importance across 10 permutations. (b) Evolution of the overall accuracy and F-scores of the classes based on the input data for the classification. Mean spatial filter = mean of pixel values in 3 × 3, 5 × 5 and 7 × 7 moving windows. Homogeneity = texture attribute 'homogeneity' based on the gray-level co-occurrence matrix applied within a 21 × 21 moving window. Domain knowledge reevaluation = refinement using elevation differences and model scores to ensure alignment with domain knowledge (see **section 2.4**). majority filter = filter using windows of increasing size up to 11 × 11 pixels, to reduce noise and enhance classification consistency.

https://doi.org/10.5194/egusphere-2025-3788
Preprint. Discussion started: 15 August 2025

Table C. 1: Confusion matrix for the classification model & precision, recall and F-score for each cover class after classes aggregation for 2019. This model uses 55 bands as input data, namely (i) 11 bands with original data (3 spectral bands, relative elevation and slope for the years 2019 and 2021 as well as the difference in relative elevation between 2019 and 2021) along with (ii) 3 × 11 bands with spatial filters (mean & standard deviation) over windows of increasing size, i.e. 3 × 3, 5 × 5 and 7 × 7, and finally (iii) the 11 bands from the texture attribute 'homogeneity'. The classification output was then filtered with a moving window of 11 × 11 pixels.

		Predicted							
		other	stable palsa	undergoing degradation	degraded areas		Precision	Recall	F-score
actual	other	**60**	2	3	5	70	86%	86%	86%
	stable palsa	5	**242**	8	33	288	84%	73%	78%
	undergoing degradation	2	33	**50**	34	119	42%	57%	49%
	degraded areas	3	56	26	**736**	821	90%	91%	90%
		70	333	87	808	1298			

Table C. 2: Confusion matrix for the classification model & precision, recall and F-score for each cover class after classes aggregation for 2021. This model uses 55 bands as input data, namely (i) 11 bands with original data (3 spectral bands, relative elevation and slope for the years 2019 and 2021 as well as the difference in relative elevation between 2019 and 2021) along with (ii) 3 × 11 bands with spatial filters (mean & standard deviation) over windows of increasing size, i.e. 3 × 3, 5 × 5 and 7 × 7, and finally (iii) the 11 bands from the texture attribute 'homogeneity'. The classification output was then filtered with a moving window of 11 × 11 pixels.

		Predicted							
		other	stable palsa	undergoing degradation	degraded areas		Precision	Recall	F-score
actual	other	**60**	1	4	5	*70*	86%	86%	86%
	stable palsa	4	**216**	5	27	*252*	86%	74%	79%
	undergoing degradation	2	20	**37**	29	*88*	42%	55%	48%
	degraded areas	4	55	21	**808**	*888*	91%	93%	92%
		70	*292*	*67*	*869*	1298			

https://doi.org/10.5194/egusphere-2025-3788
Preprint. Discussion started: 15 August 2025

Code availability

The code for the biennial model (2019-2021) is available on https://doi.org/10.14428/DVN/SX6TYV (Open Data @ UCLouvain, V1).

Data availability

All digital data, i.e. orthomosaics and digital elevation models, are available:

- 2014: Palace, M., Herrick, C., DelGreco, J., Varner, R.K., Finnell, D., Garnello, A.J. (2019). Unmanned Aerial Imagery over Stordalen Mire, Northern Sweden, 2014, https://doi.org/10.7910/DVN/SJKV4T, *Harvard Dataverse*, V1
- 2015: Palace, M., DelGreco, J., McArthur, K., Herrick, C., Varner, R.K. (2022a). Unmanned Aerial Imagery over Stordalen Mire, Northern Sweden, 2015, https://doi.org/10.7910/DVN/NUXE30, *Harvard Dataverse*, V1
- 2016: Palace, M., Herrick, C., Varner, R.K. (2022b). Unmanned Aerial Imagery over Stordalen Mire, Northern Sweden, 2016, https://doi.org/10.7910/DVN/IAXSRD, *Harvard Dataverse*, V1
- 2017: DelGreco, J., Palace, M., Herrick, C., Varner, R.K. (2022). Unmanned Aerial Imagery over Stordalen Mire, Northern Sweden, 2017, https://doi.org/10.7910/DVN/NZWLHE, *Harvard Dataverse*, V1
- 2018: Palace, M., Herrick, C., Sullivan, F. (2025a). Unmanned Aerial Imagery over Stordalen Mire, Northern Sweden, 2018. https://doi.org/10.7910/DVN/2JXWVW, *Harvard Dataverse*, V1
- 2019: Siewert, M. - Abisko Scientific Research Station (2020). UAV - RGB orthomosaic from Stordalen, 2019-08-16. *Swedish Infrastructure for Ecosystem Science (SITES)*. https://hdl.handle.net/11676.1/U4o8KrPkEiKw5RsfiCJZeEgX
- 2021: Thomas, Maxime; Villani, Maëlle; du Bois d'Aische, Eléonore; Hirst, Catherine; Lundin, Erik; Van Oost, Kristof; Vanacker, Veerle; Opfergelt, Sophie, 2025, "RGB orthomosaic, digital surface model and slope over Stordalen Mire, Northern Sweden, 2021", https://doi.org/10.14428/DVN/MGNYNN, Open Data @ UCLouvain, V1
- 2022: Palace, M., Herrick, C., Sullivan, F., Varner, R., (2025b). Unmanned Aerial Imagery over Stordalen Mire, Northern Sweden, 2022. https://doi.org/10.7910/DVN/G9Y8WC, *Harvard Dataverse*, V1

Author contribution

MT, EdBdA, MV, CH, EL and SO took part in the fieldwork in September 2021. MT carried out the UAS flights for 2021. KVO and VV provided UAS expertise and help on fieldwork preparation. MWP, RKV, CH and FBS provided UAS-derived data from 2014 to 2018 and 2022 and expertise on the study area. MBS provided UAS-derived data from 2019. JR, BD, FJ

https://doi.org/10.5194/egusphere-2025-3788
Preprint. Discussion started: 15 August 2025

and MBS provided remote sensing expertise. SL provided guidance on electromagnetic induction data acquisition and interpretation. EL and CMM contributed with their expertise on the study area. MT and TM performed the data processing. MT wrote the manuscript under supervision of SO with inputs from all co-authors.

Competing interests

The authors declare that they have no known competing financial interests or personal relationships that could have appeared to influence the work reported in this paper.

Acknowledgements

The authors are greatful to 'Länsstyrelsen Norrbotten' for allowing this scientific research in the Stordalens naturreservat. This project has benefited from collaboration with the members of the project LandSense funded by the Federation Wallonie-Bruxelles (Action de Recherche Concertée no. 21/26–119). Sophia A. Burke is acknowledged for her contribution of UAS imagery from 2022. Jennie Wikström, Annika Kristoffersson and Niklas Rakos are acknowledged for precious help on the field. We thank the Swedish Polar Research Secretariat, The Integrated Carbon Observation System (ICOS) and the Swedish Infrastructure for Ecosystem Science (SITES) for the support of the work done at the Abisko Scientific Research Station. Rose Paque and He Zhang are acknowledged for help in fieldwork preparation. Arthur Monhonval and Elisabeth Mauclet are acknowledged for data collection and useful discussions. MT thanks the members of the ELIe-SOIL lab for useful critical comments. MT is also grateful to Nicolas Deffense and Boris Nörgaard for their advice on the code.

Financial support

This project received funding from the European Union's Horizon 2020 research and innovation program under grant agreement No.714617 to SO (WeThaw), and SO acknowledges funding from the Fund for Scientific Research FNRS in Belgium (FC69480). UAS-derived data from 2014 to 2018 and 2022 were supported through the following grants to RKV: The Northern Ecosystems Research for Undergraduates program (NERU; National Science Foundation REU site EAR-1063037), MacroSystems Biology grant (NSF EF #1241037), NASA Interdisciplinary Science grant (NASA #NNX17AK10G), U.S. Department of Energy grant (DE-SC0016440) and the U.S. National Science Foundation EMERGE Biological Integration Institute grant (DBI-2022070).

https://doi.org/10.5194/egusphere-2025-3788
Preprint. Discussion started: 15 August 2025

References

AMAP: Arctic Climate Change Update 2021: Key Trends and Impacts. Summary for Policy-makers, Arctic Monitoring and Assessment Programme (AMAP), Tromsø, Norway, 2021.

Arndt, S., Jørgensen, B. B., LaRowe, D. E., Middelburg, J. J., Pancost, R. D., and Regnier, P.: Quantifying the degradation of organic matter in marine sediments: A review and synthesis, Earth-Science Reviews, 123, 53–86, https://doi.org/10.1016/j.earscirev.2013.02.008, 2013.

de la Barreda-Bautista, B., Boyd, D. S., Ledger, M., Siewert, M. B., Chandler, C., Bradley, A. V., Gee, D., Large, D. J., Olofsson, J., Sowter, A., and Sjögersten, S.: Towards a Monitoring Approach for Understanding Permafrost Degradation and Linked Subsidence in Arctic Peatlands, Remote Sensing, 14, 444, https://doi.org/10.3390/rs14030444, 2022.

Barry, R. G. and Hall-McKim, E. A.: Polar Environments and Global Change, Cambridge University Press, 445 pp., 2018.

Borge, A. F., Westermann, S., Solheim, I., and Etzelmüller, B.: Strong degradation of palsas and peat plateaus in northern Norway during the last 60 years, The Cryosphere, 11, 1–16, https://doi.org/10.5194/tc-11-1-2017, 2017.

Bosiö, J., Johansson, M., Callaghan, T. V., Johansen, B., and Christensen, T. R.: Future vegetation changes in thawing subarctic mires and implications for greenhouse gas exchange—a regional assessment, Climatic Change, 115, 379–398, https://doi.org/10.1007/s10584-012-0445-1, 2012.

Brooker, A., Fraser, R. H., Olthof, I., Kokelj, S. V., and Lacelle, D.: Mapping the Activity and Evolution of Retrogressive Thaw Slumps by Tasselled Cap Trend Analysis of a Landsat Satellite Image Stack, Permafrost and Periglacial Processes, 25, 243–256, https://doi.org/10.1002/ppp.1819, 2014.

Burke, S. A., Wik, M., Lang, A., Contosta, A. R., Palace, M., Crill, P. M., and Varner, R. K.: Long-Term Measurements of Methane Ebullition From Thaw Ponds, Journal of Geophysical Research: Biogeosciences, 124, 2208–2221, https://doi.org/10.1029/2018JG004786, 2019.

Burn, C. R. and Lewkowicz, A. G.: Canadian Landform Examples - Retrogressive Thaw Slumps, Can. Geogr., 34, 273–276, https://doi.org/10.1111/j.1541-0064.1990.tb01092.x, 1990.

Callaghan, T. V., Bergholm, F., Christensen, T. R., Jonasson, C., Kokfelt, U., and Johansson, M.: A new climate era in the sub-Arctic: Accelerating climate changes and multiple impacts, Geophysical Research Letters, 37, https://doi.org/10.1029/2009GL042064, 2010.

Canadell, J. G., Monteiro, P. M. S., Costa, M. H., Cotrim da Cunha, L., Cox, P. M., Eliseev, A. V., Henson, S., Ishii, M., Jaccard, J., Koven, C., Lohila, A., Patra, P. K., Piao, S., Rogelj, J., Syampungani, S., Zaehle, S., and Zickfeld, K.: Global Carbon and other Biogeochemical Cycles and Feedbacks., in: Climate Change 2021: The Physical Science Basis., edited by: Masson-Delmotte, V., Zhai, P., Pirani, A., Connors, S. L., Péan, C., Berger, S., Caud, N., Chen, Y., Goldfarb, L., Gomis, M. I., Huang, M., Leitzell, K., Lonnoy, E., Matthews, J. B. R., Maycock, T. K., Waterfield, T., Yelekçi, O., Yu, R., and Zhou, B., Cambridge, United Kingdom and New York, NY, USA, 673–816, https://doi.org/10.1017/9781009157896.007, 2021.

Canfield, D. E.: Factors influencing organic carbon preservation in marine sediments, Chemical Geology, 114, 315–329, https://doi.org/10.1016/0009-2541(94)90061-2, 1994.

Chang, K.-Y., Riley, W. J., Crill, P. M., Grant, R. F., Rich, V. I., and Saleska, S. R.: Large carbon cycle sensitivities to climate across a permafrost thaw gradient in subarctic Sweden, The Cryosphere, 13, 647–663, https://doi.org/10.5194/tc-13-647-2019, 2019a.

https://doi.org/10.5194/egusphere-2025-3788
Preprint. Discussion started: 15 August 2025

Chang, K.-Y., Riley, W. J., Brodie, E. L., McCalley, C. K., Crill, P. M., and Grant, R. F.: Methane Production Pathway Regulated Proximally by Substrate Availability and Distally by Temperature in a High-Latitude Mire Complex, Journal of Geophysical Research: Biogeosciences, 124, 3057–3074, https://doi.org/10.1029/2019JG005355, 2019b.

Chasmer, L. and Hopkinson, C.: Threshold loss of discontinuous permafrost and landscape evolution, Global Change Biology, 23, 2672–2686, https://doi.org/10.1111/gcb.13537, 2017.

Christensen, T. R., Johansson, T., Åkerman, H. J., Mastepanov, M., Malmer, N., Friborg, T., Crill, P., and Svensson, B. H.: Thawing sub-arctic permafrost: Effects on vegetation and methane emissions, Geophysical Research Letters, 31, https://doi.org/10.1029/2003GL018680, 2004.

Czaplewski, R. L. and Catts, G. P.: Calibration of remotely sensed proportion or area estimates for misclassification error, Remote Sensing of Environment, 39, 29–43, https://doi.org/10.1016/0034-4257(92)90138-A, 1992.

DelGreco, J.: Four Years of Unmanned Aerial System Imagery Reveals Vegetation Change in a Sub-Arctic Mire Due to Permafrost Thaw, Master Thesis, University of New Hampshire, Durham, NH 03824, USA, 48 pp., 2018.

DelGreco, J., Palace, M. W., Herrick, C., and Varner, R. K.: Unmanned Aerial Imagery over Stordalen Mire, Northern Sweden, 2017, https://doi.org/10.7910/DVN/NZWLHE, 2022.

Doolittle, J. A. and Brevik, E. C.: The use of electromagnetic induction techniques in soils studies, Geoderma, 223–225, 33–45, https://doi.org/10.1016/j.geoderma.2014.01.027, 2014.

Esri and Maxar: "World Imagery" [basemap]., https://services.arcgisonline.com/ArcGIS/rest/services/World_Imagery/MapServer, 2022.

Farquharson, L. M., Romanovsky, V. E., Cable, W. L., Walker, D. A., Kokelj, S. V., and Nicolsky, D.: Climate Change Drives Widespread and Rapid Thermokarst Development in Very Cold Permafrost in the Canadian High Arctic, Geophysical Research Letters, 46, 6681–6689, https://doi.org/10.1029/2019GL082187, 2019.

Fewster, R. E., Morris, P. J., Ivanovic, R. F., Swindles, G. T., Peregon, A. M., and Smith, C. J.: Imminent loss of climate space for permafrost peatlands in Europe and Western Siberia, Nat. Clim. Chang., 12, 373–379, https://doi.org/10.1038/s41558-022-01296-7, 2022.

Fox-Kemper, B., Hewitt, H. T., Xiao, C., Aðalgeirsdóttir, G., Drijfhout, S. S., Edwards, T. L., Golledge, N. R., Hemer, M., Koop, R. E., Krinner, G., Mix, A., Notz, D., Nowicki, S., Nurhati, I. S., Ruiz, L., Sallée, J.-B., Slangen, A. B. A., and Yu, Y.: Ocean, Cryosphere and Sea Level Change, in: Climate Change 2021: The Physical Science Basis. Contribution of Working Group I to the Sixth Assessment Report of the Intergovernmental Panel on Climate Change, edited by: Masson-Delmotte, V., Zhai, P., Pirani, A., Connors, S. L., Péan, C., Berger, S., Caud, N., Chen, Y., Goldfarb, L., Gomis, M. I., Huang, M., Leitzell, K., Lonnoy, E., Matthews, J. B. R., Maycock, T. K., Waterfield, T., Yelekçi, O., Yu, R., and Zhou, B., Cambridge University Press, Cambridge, United Kingdom and New York, NY, USA, 1211–1362, https://doi.org/10.1017/9781009157896.011, 2021.

Fuchs, M., Kuhry, P., and Hugelius, G.: Low below-ground organic carbon storage in a subarctic Alpine permafrost environment, The Cryosphere, 9, 427–438, https://doi.org/10.5194/tc-9-427-2015, 2015.

Godin, E. and Fortier, D.: Geomorphology of a thermo-erosion gully, Bylot Island, Nunavut, Canada1This article is one of a series of papers published in this CJES Special Issue on the theme of Fundamental and applied research on permafrost in Canada.2Polar Continental Shelf Project Contribution 043-11., Can. J. Earth Sci., 49, 979–986, https://doi.org/10.1139/e2012-015, 2012.

https://doi.org/10.5194/egusphere-2025-3788
Preprint. Discussion started: 15 August 2025

Grosse, G., Schirrmeister, L., and Malthus, T. J.: Application of Landsat-7 satellite data and a DEM for the quantification of thermokarst-affected terrain types in the periglacial Lena–Anabar coastal lowland, Polar Research, 25, 51–67, https://doi.org/10.3402/polar.v25i1.6238, 2006.

Hall-Beyer, M.: Practical guidelines for choosing GLCM textures to use in landscape classification tasks over a range of moderate spatial scales, International Journal of Remote Sensing, 38, 1312–1338, https://doi.org/10.1080/01431161.2016.1278314, 2017.

Haralick, R. M.: Statistical and structural approaches to texture, Proceedings of the IEEE, 67, 786–804, https://doi.org/10.1109/PROC.1979.11328, 1979.

Haralick, R. M., Shanmugam, K., and Dinstein, I.: Textural Features for Image Classification, IEEE Transactions on Systems, Man, and Cybernetics, SMC-3, 610–621, https://doi.org/10.1109/TSMC.1973.4309314, 1973.

Hay, A. M.: The derivation of global estimates from a confusion matrix, International Journal of Remote Sensing, 9, 1395–1398, https://doi.org/10.1080/01431168808954945, 1988.

Heginbottom, J. A., Brown, J., Humlum, O., and Svensson, H.: Permafrost and Periglacial Environments, in: State of the Earth's cryosphere at the beginning of the 21st century : glaciers, global snow cover, floating ice, and permafrost and periglacial environments, U.S. Geological Survey, Reston, VA, A425–A496, 2012.

Heil, K. and Schmidhalter, U.: The Application of EM38: Determination of Soil Parameters, Selection of Soil Sampling Points and Use in Agriculture and Archaeology, Sensors, 17, 2540, https://doi.org/10.3390/s17112540, 2017.

Hemingway, J. D., Rothman, D. H., Grant, K. E., Rosengard, S. Z., Eglinton, T. I., Derry, L. A., and Galy, V. V.: Mineral protection regulates long-term global preservation of natural organic carbon, Nature, 570, 228–231, https://doi.org/10.1038/s41586-019-1280-6, 2019.

Henrion, M., Li, Y., Koganti, T., Bechtold, M., Jonard, F., Opfergelt, S., Vanacker, V., Van Oost, K., and Lambot, S.: Mapping and monitoring peatlands in the Belgian Hautes Fagnes: Insights from Ground-penetrating radar and Electromagnetic induction characterization, Geoderma Regional, 37, e00795, https://doi.org/10.1016/j.geodrs.2024.e00795, 2024.

Hodgkins, S. B., Tfaily, M. M., McCalley, C. K., Logan, T. A., Crill, P. M., Saleska, S. R., Rich, V. I., and Chanton, J. P.: Changes in peat chemistry associated with permafrost thaw increase greenhouse gas production, PNAS, 111, 5819–5824, https://doi.org/10.1073/pnas.1314641111, 2014.

Hugelius, G., Tarnocai, C., Broll, G., Canadell, J. G., Kuhry, P., and Swanson, D. K.: The Northern Circumpolar Soil Carbon Database: spatially distributed datasets of soil coverage and soil carbon storage in the northern permafrost regions, Earth System Science Data, 5, 3–13, https://doi.org/10.5194/essd-5-3-2013, 2013.

Hugelius, G., Strauss, J., Zubrzycki, S., Harden, J. W., Schuur, E. a. G., Ping, C.-L., Schirrmeister, L., Grosse, G., Michaelson, G. J., Koven, C. D., O'Donnell, J. A., Elberling, B., Mishra, U., Camill, P., Yu, Z., Palmtag, J., and Kuhry, P.: Estimated stocks of circumpolar permafrost carbon with quantified uncertainty ranges and identified data gaps, Biogeosciences, 11, 6573–6593, https://doi.org/10.5194/bg-11-6573-2014, 2014.

Hugelius, G., Loisel, J., Chadburn, S., Jackson, R. B., Jones, M., MacDonald, G., Marushchak, M., Olefeldt, D., Packalen, M., Siewert, M. B., Treat, C., Turetsky, M., Voigt, C., and Yu, Z.: Large stocks of peatland carbon and nitrogen are vulnerable to permafrost thaw, Proceedings of the National Academy of Sciences, 117, 20438–20446, https://doi.org/10.1073/pnas.1916387117, 2020.

van Huissteden, J., Teshebaeva, K., Cheung, Y., Magnússon, R. Í., Noorbergen, H., Karsanaev, S. V., Maximov, T. C., and Dolman, A. J.: Geomorphology and InSAR-Tracked Surface Displacements in an Ice-Rich Yedoma Landscape, Front. Earth Sci., 9, https://doi.org/10.3389/feart.2021.680565, 2021.

Johansson, T., Malmer, N., Crill, P. M., Friborg, T., Åkerman, J. H., Mastepanov, M., and Christensen, T. R.: Decadal vegetation changes in a northern peatland, greenhouse gas fluxes and net radiative forcing, Global Change Biology, 12, 2352–2369, https://doi.org/10.1111/j.1365-2486.2006.01267.x, 2006.

Keil, R. G. and Mayer, L. M.: Mineral Matrices and Organic Matter, in: Treatise on Geochemistry (Second Edition), edited by: Holland, H. D. and Turekian, K. K., Elsevier, Oxford, 337–359, https://doi.org/10.1016/B978-0-08-095975-7.01024-X, 2014.

Kokelj, S. V. and Jorgenson, M. T.: Advances in Thermokarst Research, Permafr. Periglac. Process., 24, 108–119, https://doi.org/10.1002/ppp.1779, 2013.

Kokelj, S. V., Lantz, T. C., Tunnicliffe, J., Segal, R., and Lacelle, D.: Climate-driven thaw of permafrost preserved glacial landscapes, northwestern Canada, Geology, 45, 371–374, https://doi.org/10.1130/G38626.1, 2017.

Kokelj, S. V., Kokoszka, J., van der Sluijs, J., Rudy, A. C. A., Tunnicliffe, J., Shakil, S., Tank, S. E., and Zolkos, S.: Thaw-driven mass wasting couples slopes with downstream systems, and effects propagate through Arctic drainage networks, The Cryosphere, 15, 3059–3081, https://doi.org/10.5194/tc-15-3059-2021, 2021.

Lacelle, D., Brooker, A., Fraser, R. H., and Kokelj, S. V.: Distribution and growth of thaw slumps in the Richardson Mountains–Peel Plateau region, northwestern Canada, Geomorphology, 235, 40–51, https://doi.org/10.1016/j.geomorph.2015.01.024, 2015.

Łakomiec, P., Holst, J., Friborg, T., Crill, P., Rakos, N., Kljun, N., Olsson, P.-O., Eklundh, L., Persson, A., and Rinne, J.: Field-scale CH4 emission at a subarctic mire with heterogeneous permafrost thaw status, Biogeosciences, 18, 5811–5830, https://doi.org/10.5194/bg-18-5811-2021, 2021.

Lamoureux, S. F. and Lafrenière, M. J.: Fluvial Impact of Extensive Active Layer Detachments, Cape Bounty, Melville Island, Canada, Arctic, Antarctic, and Alpine Research, 41, 59–68, https://doi.org/10.1657/1523-0430-41.1.59, 2009.

Lantz, T. C. and Kokelj, S. V.: Increasing rates of retrogressive thaw slump activity in the Mackenzie Delta region, N.W.T., Canada, Geophysical Research Letters, 35, https://doi.org/10.1029/2007GL032433, 2008.

Lehmann, J. and Kleber, M.: The contentious nature of soil organic matter, Nature, 528, 60–68, https://doi.org/10.1038/nature16069, 2015.

Leppiniemi, O., Karjalainen, O., Aalto, J., Luoto, M., and Hjort, J.: Environmental spaces for palsas and peat plateaus are disappearing at a circumpolar scale, The Cryosphere, 17, 3157–3176, https://doi.org/10.5194/tc-17-3157-2023, 2023.

Lewkowicz, A. G.: Dynamics of active-layer detachment failures, Fosheim Peninsula, Ellesmere Island, Nunavut, Canada, Permafr. Periglac. Process., 18, 89–103, https://doi.org/10.1002/ppp.578, 2007.

Lewkowicz, A. G. and Way, R. G.: Extremes of summer climate trigger thousands of thermokarst landslides in a High Arctic environment, Nature Communications, 10, 1329, https://doi.org/10.1038/s41467-019-09314-7, 2019.

https://doi.org/10.5194/egusphere-2025-3788
Preprint. Discussion started: 15 August 2025

Li, Q., Wang, L., Fu, Y., Lin, D., Hou, M., Li, X., Hu, D., and Wang, Z.: Transformation of soil organic matter subjected to environmental disturbance and preservation of organic matter bound to soil minerals: a review, J Soils Sediments, 23, 1485–1500, https://doi.org/10.1007/s11368-022-03381-y, 2023.

Littlefair, C. A., Tank, S. E., and Kokelj, S. V.: Retrogressive thaw slumps temper dissolved organic carbon delivery to streams of the Peel Plateau, NWT, Canada, Biogeosciences, 14, 5487–5505, https://doi.org/10.5194/bg-14-5487-2017, 2017.

von Lützow, M., Kögel-Knabner, I., Ludwig, B., Matzner, E., Flessa, H., Ekschmitt, K., Guggenberger, G., Marschner, B., and Kalbitz, K.: Stabilization mechanisms of organic matter in four temperate soils: Development and application of a conceptual model, Journal of Plant Nutrition and Soil Science, 171, 111–124, https://doi.org/10.1002/jpln.200700047, 2008.

Malone, L., Lacelle, D., Kokelj, S., and Clark, I. D.: Impacts of hillslope thaw slumps on the geochemistry of permafrost catchments (Stony Creek watershed, NWT, Canada), Chemical Geology, 356, 38–49, https://doi.org/10.1016/j.chemgeo.2013.07.010, 2013.

Mamet, S. D., Chun, K. P., Kershaw, G. G. L., Loranty, M. M., and Peter Kershaw, G.: Recent Increases in Permafrost Thaw Rates and Areal Loss of Palsas in the Western Northwest Territories, Canada, Permafrost and Periglacial Processes, 28, 619–633, https://doi.org/10.1002/ppp.1951, 2017.

Martin, L. C. P., Nitzbon, J., Scheer, J., Aas, K. S., Eiken, T., Langer, M., Filhol, S., Etzelmüller, B., and Westermann, S.: Lateral thermokarst patterns in permafrost peat plateaus in northern Norway, The Cryosphere, 15, 3423–3442, https://doi.org/10.5194/tc-15-3423-2021, 2021.

McNeill, J. D.: Electromagnetic terrain conductivity measurement at low induction numbers, Geonics Limited, Tech. Note TN-6, 8, 1980.

Meredith, M., Sommerkorn, M., Cassotta, S., Derksen, C., Ekaykin, A., Hollowed, A., Kofinas, G., Mackintosh, A., Melbourne-Thomas, J., Muelbert, M. M. C., Ottersen, G., Pritchard, H., and Schuur, E. A. G.: Polar Regions, in: IPCC Special Report on the Ocean and Cryosphere in a Changing Climate, edited by: Pörtner, H.-O., Roberts, D. C., Masson-Delmotte, V., Zhai, P., Tignor, M., Poloczanska, E., Mintenbeck, K., Alegría, A., Nicolai, M., Okem, A., Petzold, J., Rama, B., and Weyer, N. M., Cambridge University Press, Cambridge, UK and New York, NY, USA, 203–320, 2019.

Mondav, R., Woodcroft, B. J., Kim, E.-H., McCalley, C. K., Hodgkins, S. B., Crill, P. M., Chanton, J., Hurst, G. B., VerBerkmoes, N. C., Saleska, S. R., Hugenholtz, P., Rich, V. I., and Tyson, G. W.: Discovery of a novel methanogen prevalent in thawing permafrost, Nat Commun, 5, 3212, https://doi.org/10.1038/ncomms4212, 2014.

Monhonval, A., Mauclet, E., Hirst, C., Bemelmans, N., Eekman, E., Schuur, E. A. G., and Opfergelt, S.: Mineral organic carbon interactions in dry versus wet tundra soils, Geoderma, 436, 116552, https://doi.org/10.1016/j.geoderma.2023.116552, 2023.

Natali, S. M., Holdren, J. P., Rogers, B. M., Treharne, R., Duffy, P. B., Pomerance, R., and MacDonald, E.: Permafrost carbon feedbacks threaten global climate goals, Proc. Natl. Acad. Sci., 118, e2100163118, https://doi.org/10.1073/pnas.2100163118, 2021.

National Geographic, Esri, DeLorme, HERE, UNEP-WCMC, USGS, NASA, ESA, METI, NRCAN, GEBCO, NOAA, and iPC: "National Geographic World Map" [basemap]., https://services.arcgisonline.com/ArcGIS/rest/services/NatGeo_World_Map/MapServer, 2011.

https://doi.org/10.5194/egusphere-2025-3788
Preprint. Discussion started: 15 August 2025

Nicolsky, D. J., Romanovsky, V. E., Panda, S. K., Marchenko, S. S., and Muskett, R. R.: Applicability of the ecosystem type approach to model permafrost dynamics across the Alaska North Slope, Journal of Geophysical Research: Earth Surface, 122, 50–75, https://doi.org/10.1002/2016JF003852, 2017.

Nitze, I., Grosse, G., Jones, B. M., Romanovsky, V. E., and Boike, J.: Remote sensing quantifies widespread abundance of permafrost region disturbances across the Arctic and Subarctic, Nat Commun, 9, 5423, https://doi.org/10.1038/s41467-018-07663-3, 2018.

Olefeldt, D., Goswami, S., Grosse, G., Hayes, D., Hugelius, G., Kuhry, P., McGuire, A. D., Romanovsky, V. E., Sannel, A. B. K., Schuur, E. a. G., and Turetsky, M. R.: Circumpolar distribution and carbon storage of thermokarst landscapes, Nature Communications, 7, 1–11, https://doi.org/10.1038/ncomms13043, 2016.

Olvmo, M., Holmer, B., Thorsson, S., Reese, H., and Lindberg, F.: Sub-arctic palsa degradation and the role of climatic drivers in the largest coherent palsa mire complex in Sweden (Vissátvuopmi), 1955–2016, Sci Rep, 10, 8937, https://doi.org/10.1038/s41598-020-65719-1, 2020.

Palace, M., Herrick, C., DelGreco, J., Finnell, D., Garnello, A. J., McCalley, C., McArthur, K., Sullivan, F., and Varner, R. K.: Determining Subarctic Peatland Vegetation Using an Unmanned Aerial System (UAS), Remote Sensing, 10, 1498, https://doi.org/10.3390/rs10091498, 2018.

Palace, M., Herrick, C., DelGreco, J., Varner, R., Finnell, D., and Garnello, A. J.: Unmanned Aerial Imagery over Stordalen Mire, Northern Sweden, 2014, https://doi.org/10.7910/DVN/SJKV4T, 2019.

Palace, M., Herrick, C., and Sullivan, F.: Unmanned Aerial Imagery over Stordalen Mire, Northern Sweden, 2018, https://doi.org/10.7910/DVN/2JXWVW, 2025a.

Palace, M., Herrick, C., Sullivan, F., and Varner, R.: Unmanned Aerial Imagery over Stordalen Mire, Northern Sweden, 2022, https://doi.org/10.7910/DVN/G9Y8WC, 2025b.

Palace, M. W., DelGreco, J., McArthur, K., Herrick, C., and Varner, R. K.: Unmanned Aerial Imagery over Stordalen Mire, Northern Sweden, 2015, https://doi.org/10.7910/DVN/NUXE30, 2022a.

Palace, M. W., Herrick, C., and Varner, R. K.: Unmanned Aerial Imagery over Stordalen Mire, Northern Sweden, 2016, https://doi.org/10.7910/DVN/IAXSRD, 2022b.

Palmtag, J., Hugelius, G., Lashchinskiy, N., Tamstorf, M. P., Richter, A., Elberling, B., and Kuhry, P.: Storage, Landscape Distribution, and Burial History of Soil Organic Matter in Contrasting Areas of Continuous Permafrost, Arctic, Antarctic, and Alpine Research, 47, 71–88, https://doi.org/10.1657/AAAR0014-027, 2015.

Patzner, M. S., Mueller, C. W., Malusova, M., Baur, M., Nikeleit, V., Scholten, T., Hoeschen, C., Byrne, J. M., Borch, T., Kappler, A., and Bryce, C.: Iron mineral dissolution releases iron and associated organic carbon during permafrost thaw, Nat Commun, 11, 6329, https://doi.org/10.1038/s41467-020-20102-6, 2020.

Porter, C., Howat, I., Noh, M.-J., Husby, E., Khuvis, S., Danish, E., Tomko, K., Gardiner, J., Negrete, A., Yadav, B., Klassen, J., Kelleher, C., Cloutier, M., Bakker, J., Enos, J., Arnold, G., Bauer, G., and Morin, P.: ArcticDEM - Mosaics, Version 4.1, Harvard Dataverse, V1, 2023.

Rantanen, M., Karpechko, A. Y., Lipponen, A., Nordling, K., Hyvärinen, O., Ruosteenoja, K., Vihma, T., and Laaksonen, A.: The Arctic has warmed nearly four times faster than the globe since 1979, Commun Earth Environ, 3, 1–10, https://doi.org/10.1038/s43247-022-00498-3, 2022.

https://doi.org/10.5194/egusphere-2025-3788
Preprint. Discussion started: 15 August 2025

Renette, C., Olvmo, M., Thorsson, S., Holmer, B., and Reese, H.: Multitemporal UAV lidar detects seasonal heave and subsidence on palsas, The Cryosphere, 18, 5465–5480, https://doi.org/10.5194/tc-18-5465-2024, 2024.

Rodenhizer, H., Belshe, F., Celis, G., Ledman, J., Mauritz, M., Goetz, S., Sankey, T., and Schuur, E. A. G.: Abrupt permafrost thaw accelerates carbon dioxide and methane release at a tussock tundra site, Arctic, Antarctic, and Alpine Research, 54, 443–464, https://doi.org/10.1080/15230430.2022.2118639, 2022.

Siewert, M. B.: High-resolution digital mapping of soil organic carbon in permafrost terrain using machine learning: a case study in a sub-Arctic peatland environment, Biogeosciences, 15, 1663–1682, https://doi.org/10.5194/bg-15-1663-2018, 2018.

Siewert, M. B. and Abisko Scientific Research Station: RGB orthomosaic and digital surface model from Stordalen 2019-08-16, Swedish Infrastructure for Ecosystem Science (SITES), https://hdl.handle.net/11676.1/U4o8KrPkEiKw5RsfiCJZeEgX, 2020.

Siewert, M. B., Hugelius, G., Heim, B., and Faucherre, S.: Landscape controls and vertical variability of soil organic carbon storage in permafrost-affected soils of the Lena River Delta, CATENA, 147, 725–741, https://doi.org/10.1016/j.catena.2016.07.048, 2016.

Siewert, M. B., Lantuit, H., Richter, A., and Hugelius, G.: Permafrost Causes Unique Fine-Scale Spatial Variability Across Tundra Soils, Global Biogeochemical Cycles, 35, e2020GB006659, https://doi.org/10.1029/2020GB006659, 2021.

Sjögersten, S., Ledger, M., Siewert, M., de la Barreda-Bautista, B., Sowter, A., Gee, D., Foody, G., and Boyd, D. S.: Optical and radar Earth observation data for upscaling methane emissions linked to permafrost degradation in sub-Arctic peatlands in northern Sweden, Biogeosciences, 20, 4221–4239, https://doi.org/10.5194/bg-20-4221-2023, 2023.

van der Sluijs, J., Kokelj, S. V., Fraser, R. H., Tunnicliffe, J., and Lacelle, D.: Permafrost Terrain Dynamics and Infrastructure Impacts Revealed by UAV Photogrammetry and Thermal Imaging, Remote Sensing, 10, 1734, https://doi.org/10.3390/rs10111734, 2018.

van der Sluijs, J., Kokelj, S. V., and Tunnicliffe, J. F.: Allometric scaling of retrogressive thaw slumps, The Cryosphere, 17, 4511–4533, https://doi.org/10.5194/tc-17-4511-2023, 2023.

Strauss, J., Abbott, B. W., Hugelius, G., Schuur, E. A. G., Treat, C., Fuchs, M., Schädel, C., Ulrich, M., Turetsky, M., Keuschnig, M., Biasi, C., Yang, Y., and Grosse, G.: Permafrost, in: Recarbonizing global soils – A technical manual of recommended management practices, vol. Volume 2: Hot spots and bright spots of soil organic carbon, FAO, Rome, Italy, https://doi.org/10.4060/cb6378en, 2021.

Streletskiy, D. A., Maslakov, A., Grosse, G., Shiklomanov, N. I., Farquharson, L., Zwieback, S., Iwahana, G., Bartsch, A., Liu, L., Strozzi, T., Lee, H., and Debolskiy, M. V.: Thawing permafrost is subsiding in the Northern Hemisphere—review and perspectives, Environ. Res. Lett., 20, 013006, https://doi.org/10.1088/1748-9326/ada2ff, 2025.

Thomas, M., Villani, M., du Bois d'Aische, E., Hirst, C., Lundin, E., Van Oost, K., Vanacker, V., and Opfergelt, S.: RGB orthomosaic, digital surface model and slope over Stordalen Mire, Northern Sweden, 2021, https://doi.org/10.14428/DVN/MGNYNN, 2025.

Turetsky, M. R., Abbott, B. W., Jones, M. C., Anthony, K. W., Olefeldt, D., Schuur, E. A. G., Grosse, G., Kuhry, P., Hugelius, G., Koven, C., Lawrence, D. M., Gibson, C., Sannel, A. B. K., and McGuire, A. D.: Carbon release through abrupt permafrost thaw, Nature Geoscience, 13, 138–143, https://doi.org/10.1038/s41561-019-0526-0, 2020.

https://doi.org/10.5194/egusphere-2025-3788
Preprint. Discussion started: 15 August 2025

Valman, S., Siewert, M. B., Boyd, D., Ledger, M., Gee, D., de la Barreda-Bautista, B., Sowter, A., and Sjögersten, S.: InSAR-measured permafrost degradation of palsa peatlands in northern Sweden, The Cryosphere, 18, 1773–1790, https://doi.org/10.5194/tc-18-1773-2024, 2024.

Varner, R. K., Crill, P. M., Frolking, S., McCalley, C. K., Burke, S. A., Chanton, J. P., Holmes, M. E., Isogenie Project Coordinators, Saleska, S., and Palace, M. W.: Permafrost thaw driven changes in hydrology and vegetation cover increase trace gas emissions and climate forcing in Stordalen Mire from 1970 to 2014, Philosophical Transactions of the Royal Society A: Mathematical, Physical and Engineering Sciences, 380, 20210022, https://doi.org/10.1098/rsta.2021.0022, 2022.

Vonk, J. E., Tank, S. E., Bowden, W. B., Laurion, I., Vincent, W. F., Alekseychik, P., Amyot, M., Billet, M. F., Canário, J., Cory, R. M., Deshpande, B. N., Helbig, M., Jammet, M., Karlsson, J., Larouche, J., MacMillan, G., Rautio, M., Walter Anthony, K. M., and Wickland, K. P.: Reviews and syntheses: Effects of permafrost thaw on Arctic aquatic ecosystems, Biogeosciences, 12, 7129–7167, https://doi.org/10.5194/bg-12-7129-2015, 2015.

Winstrup, M., Ranndal, H., Larsen, S. H., Simonsen, S. B., Mankoff, K. D., Fausto, R. S., and Sørensen, L. S.: PRODEM: An annual series of summer DEMs (2019-2023) for the marginal areas of the Greenland Ice Sheet, General Assembly 2024 of the European Geosciences Union (EGU), Vienna, Austria, https://doi.org/10.5194/egusphere-egu24-5136, 2024.

Wu, K. and Lambot, S.: Analysis of Low-Frequency Drone-Borne GPR for Root-Zone Soil Electrical Conductivity Characterization, IEEE Transactions on Geoscience and Remote Sensing, 60, 1–13, https://doi.org/10.1109/TGRS.2022.3198431, 2022.

Wu, K., Rodriguez, G. A., Zajc, M., Jacquemin, E., Clément, M., De Coster, A., and Lambot, S.: A new drone-borne GPR for soil moisture mapping, Remote Sensing of Environment, 235, 111456, https://doi.org/10.1016/j.rse.2019.111456, 2019.

Yang, Y., Rogers, B. M., Fiske, G., Watts, J., Potter, S., Windholz, T., Mullen, A., Nitze, I., and Natali, S. M.: Mapping retrogressive thaw slumps using deep neural networks, Remote Sensing of Environment, 288, 113495, https://doi.org/10.1016/j.rse.2023.113495, 2023.

Zhang, H., Aldana-Jague, E., Clapuyt, F., Wilken, F., Vanacker, V., and Van Oost, K.: Evaluating the potential of post-processing kinematic (PPK) georeferencing for UAV-based structure- from-motion (SfM) photogrammetry and surface change detection, Earth Surface Dynamics, 7, 807–827, https://doi.org/10.5194/esurf-7-807-2019, 2019.

Zolkos, S. and Tank, S. E.: Permafrost geochemistry and retrogressive thaw slump morphology (Peel Plateau, Canada), v. 1.0 (2017-2017), https://doi.org/10.5885/45573XD-28DD57D553F14BF0, 2019.

Zolkos, S. and Tank, S. E.: Experimental Evidence That Permafrost Thaw History and Mineral Composition Shape Abiotic Carbon Cycling in Thermokarst-Affected Stream Networks, Front. Earth Sci., 8, https://doi.org/10.3389/feart.2020.00152, 2020.

Zolkos, S., Tank, S. E., and Kokelj, S. V.: Mineral Weathering and the Permafrost Carbon-Climate Feedback, Geophysical Research Letters, 45, 9623–9632, https://doi.org/10.1029/2018GL078748, 2018.